

Very Long Baseline Interferometry Study of the Relativistic Jet in Active Galactic Nucleus 4C+21.78

Indy Leclercq

Year in Europe Project
Imperial College London MSci Physics

Universidad de Valencia
Departamento de Astronomía y Astrofísica

Supervisor:
Professor Eduardo ROS

*Imperial College Visiting
Supervisor:*
Professor Peter TÖRÖK

24th June 2011

Contents

1	Introduction	2
2	Theoretical Background	6
2.1	Active Galactic Nuclei and Relativistic Jets	6
2.1.1	Active Galactic Nuclei	6
2.1.2	Relativistic Jets	12
2.2	Interferometry and VLBI	17
2.2.1	Interferometry : Fundamental Concepts	17
2.2.2	Aperture Synthesis	22
2.2.3	Very Long Baseline Interferometry and the VLBA	23
2.3	Object of study : 4C+21.35	24
3	Imaging and data treatment	28
3.1	Data reduction	29
3.1.1	Calibration	29
3.1.2	“Cleaning” and image production	30
3.2	Modelfitting	32
4	Results and Analysis	35
4.1	Brightness maps	35
4.2	Model components	38
5	Summary and Conclusions	52

Chapter 1

Introduction

While the observation and study of the sky dates back thousands of years, probably to the very first humans, until comparatively recently astronomical observations only took place in the narrow bandwidth of visible light. The discovery of an extraterrestrial source of radio emission by Jansky (1933) was the first step of a discipline that is now at the forefront of modern astronomy. Jansky, looking for possible sources of radio interference for voice communications, realised that a continuous background hiss varied slowly with the sidereal day. He realised that this was coming from beyond the Earth, and was centered in the constellation of Sagittarius. This source is now known as Sgr A, and is believed to originate from the center of our own galaxy, the Milky Way.

The concept of radio astronomy seemed exotic to physicists at the time, but with the development of radar technology during the second world war, many scientists started turning towards this nascent field post-1945. Progress was made in leaps and bounds, and by the mid-1950s the foundations were laid, with the detection of the 21cm Hydrogen emission line in 1952 being the first major success. The discovery of more intriguing objects, such as pulsars and quasars, followed suit; arguably the greatest discovery made using radio astronomy was the detection of the cosmic microwave background by Penzias and Wilson (1965).

Radio astronomy, as it was quickly realized, has the enormous benefit of being unaffected by the atmosphere: radio emission has a very large atmospheric “window” (see Figure 1.1) for which there is no atmospheric absorption of the radiation. 1.1 also shows the other wavebands at which astronomy is now practiced; indeed, the advent of radio observations made astronomers realize that there was much to learn from making observations at various wavelengths. X-rays and gamma-rays do not penetrate the atmosphere, however, and a number of satellite telescope, including most recently the Fermi Large Area Telescope, have been sent up to peer at the universe.

As mentioned, Jansky’s source was in fact found to be the centre of the Milky Way. The brightest known radio sources in the sky are mainly *extragalactic* in origin, though,

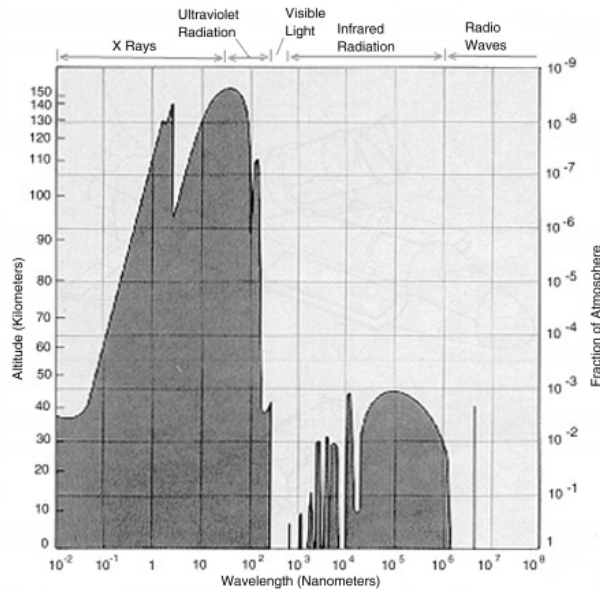


Figure 1.1: An illustration of the "windows" in the atmosphere, and the absorbed wavelengths over the EM spectrum. The upper boundaries of the grey areas represent the altitude at which incoming radiation intensity is divided by 2. The large radio window is clearly visible. Image from <http://www.sns.ias.edu/~jnb/Papers/Popular/Hstsciamerspitzer/hstsciamerspitzer.html>, originally from Scientific American, July 1982.

and many of them can be optically identified with known galaxies. Figure 1.2 shows a map of the radio sky taken at 408 MHz (73 cm), where the plane of the Milky Way runs through the center and is the most visible object. No stars can be seen, however individual objects outside the plane can be distinguished: these are the extragalactic sources, either supernova remnants, pulsars, or *Active Galactic Nuclei*.

Carl Seyfert discovered the first type of "active galaxies", which now bear his name, in 1943. Seyfert galaxies are galaxies with extremely bright cores and distinctive emission lines.

When the powerful radio source Cygnus A was optically identified in 1954 by Baade and Minkowski (1954), it was realised that it too was a bright, radio-emitting galaxy. Better and better interferometry techniques were developed, leading up to multi-element interferometry, aperture synthesis (pioneered by Martin Ryle, who received the 1974 Nobel prize for his work) and Very Long Baseline Interferometry (VLBI) (see section 2.2).

As these observational techniques progressed, more and more radio sources came to light. Many types of AGN were found, and observed at ever higher resolutions. This has led to a veritable "zoo" of AGN subtypes, which have nevertheless all been unified under a single model (see section 2.1). Sub-milliarcsecond imaging with VLBI arrays such as the North American Very Large Baseline Array (VLBA) (see section 2.2) has enabled

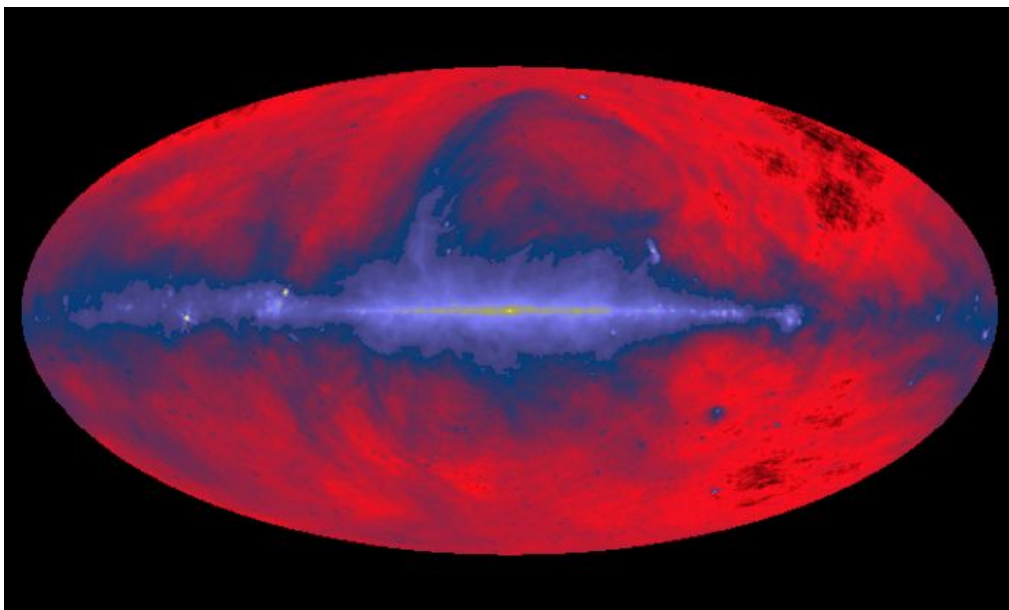


Figure 1.2: A 408 MHz image of the radio sky. This image was produced using data from the Jodrell Bank, MPIfR and Parkes Observatories. The false colour image shows the plane of the galaxy running through the center horizontally. Image credit: C.G Haslam, MPIfR

the study of a very bright and compact class of AGNs : blazars.

Blazars are observationally dominated by a large, kiloparsec scale jet of plasma, believed to be ejected by the core of the galaxy. Parsec-scale interferometry imaging of the jet has shown that it generally exhibits superluminal motion, i.e., apparent motion faster than c .

The source 4C+21.35 is studied in this report, using data from the MOJAVE AGN jet monitoring program (taken using the VLBA). The evolution of the source is studied over 8 epochs from 2008 to 2010 at a frequency of 15.3 GHz (2cm). (see also section 2.3)

4C+21.35 is a bright and compact radio source classified as a blazar by the scientific community. As stated above, it is currently monitored by the VLBA, but also by the γ -ray Fermi Large Area telescope (Atwood et al., 2009). Both telescopes have indicated a large, recent increase in emission which motivates this study for two reasons:

- It has been established that gamma-loud blazars have extremely fast-moving jets, so this source would be a prime subject for the study of superluminal motion;
- Radio and gamma flaring have been strongly correlated with the ejection of new, bright “components” or features from the core into the jet, so this new component could possibly be observed.

Furthermore, a previous kinematic study by Lister et al. (2009) is available for comparison and as an aid to evaluate the global jet behaviour.

The aim of this study is to produce brightness maps of 4C+21.35 using the raw visibility data provided by the MOJAVE team, and fit models to these to be able to describe the velocity of different areas of the blazar's jet. These (supposedly superluminal) velocities are then used to derive the viewing angle of the blazar, the true velocity of the jet and the Lorentz factor involved. The components also permit an analysis of the jet's evolution.

The theoretical background concerning AGNs and radio interferometry is presented in Chapter 2, the imaging techniques used to treat the data are shown in Chapter 3 and the maps and results are shown in Chapter 4.

Chapter 2

Theoretical Background

2.1 Active Galactic Nuclei and Relativistic Jets

2.1.1 Active Galactic Nuclei

As mentioned in the introduction, some of the brightest objects in the radio sky are what are known as Active Galactic Nuclei, or AGNs. Broadly speaking, while a normal galaxy is simply constituted of stars and interstellar matter, an *active galaxy* will also contain a very bright core which is actively emitting radiation across the electromagnetic spectrum. Often, this emission will obscure the galaxy itself, outshining it, which means that the core itself will be the object of study. While some study of host galaxies has been undertaken, it remains difficult to link the properties of an AGN with its host in a significant way (Krolik, 1999). AGNs have been found under many guises, and the plethora of categories that one may fall into initially had astronomers perplexed. However, thanks to observations made with ever-higher resolutions and an improving knowledge of the physics of AGNs, it has been possible to propose a unified model of the disparate subclasses of AGN.

General characteristics

While they are a disparate bunch, most AGNs share some common characteristics that makes it possible to identify them as such.

The predominant characteristic, as mentioned above, is their intense luminosity. AGNs have been found with luminosities ranging from $\sim 10^{42}$ erg.s⁻¹ to $\sim 10^{48}$ erg.s⁻¹. Compared with the average luminosity of a galaxy ($\sim 10^{44}$ erg.s⁻¹), the median luminosity of an AGN is about 100 times brighter.

The second distinguishing feature common to almost all AGNs is their very small angular size, on the order of a few milliarcseconds (mas) as viewed from Earth. Illustratively, Figure 2.1 shows a Seyfert galaxy, distinguished by its extremely bright and comparatively small core. The flux emitted from the central region far exceeds that of the rest of the galaxy. It must be noted however that the angular size will depend on the wavelength, and that in the case of radio sources, the emitted jets (seen later in this section) can have a greater spatial extent than the host galaxy.



Figure 2.1: An image of NGC 7742, a Seyfert type II galaxy with an active nucleus, taken at optical/UV wavelengths. Notice the extremely bright core, believed to be powered by a black hole accretion mechanism. The thick ring surrounding the core is about 1.8 kpc across. *Image credit* : NASA/ESA space observatory

Finally, a third notable feature is the broad-band continuum spectrum presented by most AGNs. Indeed, while normal galactic spectra tend to peak (emit most of their energy) within a single decade of frequency, AGNs tend to have a “flat” spectrum which can extend from the infrared to X-ray frequency domains (and can also emit at radio and gamma-ray wavelengths). This interesting property means that much information can be gleaned from AGNs by observations at different wavelengths; the emission mechanisms behind this, and possible correlations between radio and gamma-ray emissions for the object studied in this report, are explored later on. AGNs also tend to have strong emission lines in their spectra, these can be both broad and narrow. The lines make for a very distinct spectrum and set AGNs apart from other galaxies, as seen in Figure 2.2.

While the features cited above are common to most AGNs, they are stated with the caveat that few AGNs possess all of them and that other distinguishing features may only apply to a certain class of AGN (while nevertheless permitting identification of the object as such). Shared characteristics of AGNs, as well as their classification into

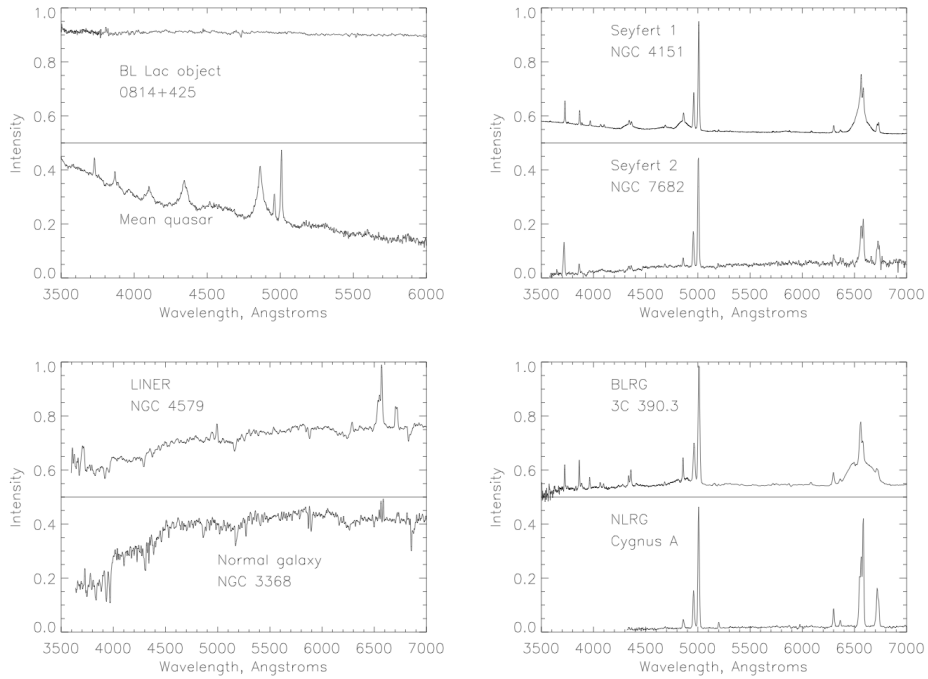


Figure 2.2: A comparison between the various spectra of different AGN classes and a normal spiral galaxy. BLRG and NLRG stand for Broad-Line and Narrow-Line Radio Galaxy, respectively. Note the presence of distinctive emission lines in every class save the BL Lac object, and the difference between the AGN spectra and the normal galaxy spectrum. Image taken from <http://www.astr.ua.edu/keel/agn/spectra.html>

subcategories and unification models (as seen in the next paragraphs) are extensively covered by Krolik (1999).

AGN categories

At first view, the various classes of AGN present a very eclectic picture - Krolik goes as far as referring to the AGN “zoo”. The terminology used for the different divisions can be confusing, due to historical reasons.

They can, firstly, be divided into two broad categories: radio-loud and radio-quiet. Radio-loud AGNs are characterised by the presence of strong radio emissions in their spectra, and include three different types of object: quasars (Quasi Stellar Radio Sources), radio galaxies and blazars. Due to the fact that radio interferometers offer the highest

resolution possible over all wavelengths, these sources are the subject of extensive study, and are some of the best-known objects in the sky.

Conversely, radio-quiet AGNs show little or no radio emission, and are made up of Seyfert galaxies, QSOs (Quasi Stellar Objects, the non-radio equivalents to quasars) and LINERs (Low Ionization Nuclear Emission Regions), whose classification as AGNs is still under debate due to uncertainty as to the radiation mechanism involved.

Of the two subclasses, radio-loud AGNs present the more interesting features, most notably the presence of large, collimated, radio-emitting jets ejected from the core. Study of the jets is helping to better understand the behaviour of AGNs and indeed of the jets themselves, as it is still unclear why they are produced. They are explored in more detail in the next section. The different types of radio-loud AGN are summarily detailed below; again, more information on these and on the radio-quiet classes is readily available in Krolik (1999).

Radio galaxies : The broadest class of radio-loud AGNs, radio galaxies were the first to be discovered, with Cygnus A in 1946 (which is still one of the brightest radio sources in the sky). They are the AGNs with the largest spatial extent, with jets sometimes extending over kiloparsec scales, exceeding the size of the host galaxy. Radio galaxies can be further subdivided into two types, FR I and FR II (after Fanaroff and Riley (1974)), according to the size and shape of the jets and lobes (situated at the end of the jets and created by the collision of the jet with surrounding diffuse gas that is part of the galaxy). A further possible distinction is between radio galaxies with broad or narrow emission lines (Figure 2.2).

Blazars : These are extremely bright radio sources whose jet forms a very small angle with the observer's line of sight. The large luminosity can be explained by the small viewing angle and by relativistic jet speeds (Doppler boosting will then occur, see next section). Blazars can be divided into two further categories : BL Lac objects, characterised by their lack of strong emission lines (Figure 2.2), and Optically Violently Variable quasars, a type of core-dominated quasar (see below) that presents strong flux variation on very short time scales (a few days or weeks). Variable emissions are also characteristic of BL Lac objects.

Quasars : Very compact, brightly emitting objects, quasars are distinguishable by their small size (parsec or even sub-parsec scale) and strong radio flux, with the presence of both broad and narrow emission lines in their spectra (Figure 2.2). Quasars, like other AGNs, have a relatively flat spectrum, and emit strongly from the optical all the way up to the gamma-ray regime. It should be noted that only about 15-20% of quasars are radio-loud, the rest are the optically/ultravioletly bright QSOs (Kellermann et al., 1989). Caution must be exercised when talking about "quasars", as usage of the term has evolved from describing compact, radio-loud AGNs to a catch-all name for active nuclei in general; some low-luminosity AGNs have come to be called "micro-quasars". Finally it can be noted that due to their high luminosity, quasars are very rare, and are generally found at very large

distances. This in turn means that quasars are usually very red-shifted.

It has proved possible, despite the apparent differences between the various classes of AGN, to construct a unified model that considers the various categories as being the same physical object, but seen under various viewing angles. This model was first proposed by Rowan-Robinson in 1977 and is being constantly refined (see also Antonucci, 1993 and Urry and Padovani, 1995)

Unification model

The single model describing all AGNs that is currently widely accepted is shown in Figure 2.3. A distinction has to be made between radio-loud and radio-quiet AGNs, however, as the latter do not possess the collimated jets that are characteristic of radio-loud AGNs. The model is comprised of a central, extremely massive object believed to be a black hole, accompanied by its accretion disk; a large, opaque molecular cloud, in the shape of a torus, surrounding the core; and in the case of radio-loud AGNs, the relativistic jets of plasma being ejected from the core.

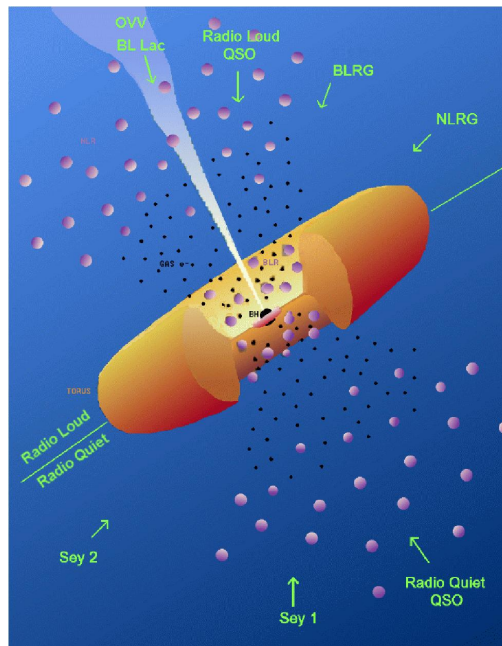


Figure 2.3: An illustration of the unified AGN model. The different classes of active nuclei are simply explained as different viewing angles of similarly constituted sources. A distinction is made between radio-loud and radio-quiet AGNs, with the radio-loud model as the top half of the image and radio-quiet as the bottom half. As shown, a very small viewing angle with respect to the AGN axis will give the image of a Blazar (or a QSO for radio-quiet nuclei), an increasing angle will show a quasar, then a Broad Line Radio Galaxy (BLRG); if the line of sight is perpendicular to the axis, a Narrow Line Radio Galaxy (NLRG) will be seen. The same model unifies QSOs, Seyfert I and Seyfert II galaxies in the same way.

The similarities and differences can now be readily understood : if the AGN is seen "head-on", directly along the axis of the jets, it is "core-dominated", and the brightness from the core overwhelms all the other components. Furthermore, the incoming jets will undergo Doppler boosting and appear even brighter to the observer. However, if the the AGN is seen "side-on", almost perpendicular to the jet, then the core is hidden from view by the obscuring torus.

Here follows a brief overview of the various parts of an AGN; more information can be found in Krolik (1999) and Burke and Graham-Smith (2002).

The "driving engine" : a black hole and its accretion disk. The sheer intensity of the radiation emitted by the core of an AGN limits the possible driving mechanisms behind the immense outflow of energy from such a comparatively small object. The process powering stellar radiation, nuclear fusion, was recognised as being far too inefficient (the conversion of Hydrogen to Helium only yields about 0.007% of the H mass as energy), and the only viable process was seen to be accretion of matter onto an extremely massive, compact object at the centre of the active galaxy; the matter does not fall directly onto the object but conserves its angular momentum and rotates around the object, forming an *accretion disk*. Such an accretion process involves the transformation of gravitational potential energy into kinetic energy, which is then released before the matter reaches the central object. Accretion releases the equivalent of about 10% of the rest mass of the falling object as energy, making it the most efficient process for mass to energy conversion known (Frank et al., 2002). Using the luminosity, and with an upper limit on the central object radius, it is possible to derive a lower limit on the mass of the object needed to sustain the accretion process (using the Eddington limit). For central objects on a sub-parsec scale, it is found that a mass of $\simeq 10^8$ is necessary. Such a large mass implies that the central object is in fact a black hole. While not fully certain, the evidence for the existence of black holes at the center of AGNs is steadily growing, Krolik (1999) outlines the main tests and evidence available.

The obscuring torus: Infrared radiation and the detection of broad and narrow emission lines in the spectra of radio galaxies imply that the areas around the accretion disk are essentially filled with gas and dust, forming a large molecular cloud. This can be divided into three regions : the broad-line region (BLR), narrow-line region (NLR) and torus. Gas close to the accretion disk is heavily perturbed by the rotation and turbulence of the accreting matter and is dispersed at very high velocities - this leads to the presence of broad emission lines in the spectrum. As seen in Figure 2.3 the NLR is an extension of the BLR, surrounding the jets as a cooler region of gas (giving narrower lines). The existence of an obscuring torus, forming an optically thick ring around the core, has been postulated following the observation of excessive infrared and maser radiation, which are strongly indicative of a molecular dust cloud (there are similar maser emissions in observed molecular clouds around some Milky Way, which enables parallels to be drawn). The torus

is also rotating around the central black hole, as has been determined by Miyoshi et al. (1995) through observations of NGC 4258.

The jets: The final element of the AGN model, for radio-loud objects, are the two antiparallel jets of matter ejected from the core. The matter is in fact believed to be plasma, travelling at relativistic speeds in a highly collimated flow. The formation process of these jets and the reason for their existence in the first place remains unknown, and is an area of considerable current interest within the field. Models have been put forward, though, and the accepted explanation so far is the formation of a helicoidal magnetic field within the accretion disk, which would then accelerate charged particles outward to form the jets, perpendicularly to the disk. The magnetic fields presumably arise from the rotation of pre-existing field lines within the disk, and the constant accretion of matter would increase the field density. Blandford and Payne (1982) showed that such a setup could theoretically explain the formation of the jets. A review of the currently favoured mechanisms for relativistic jet production has been done by Camenzind (2005). The origin of the charged particles that actually make up the jet plasma remains an unsolved problem.

The study of the relativistic jet emerging from quasar 4C 21.78 is the main objective of this report and the radio emission coming from these jets is the main observable quantity detected by the VLBI array used (see section 2.2). The following section will therefore focus on the physics and evolution of the jets, which will then enable a physical interpretation of the data gathered and presented in Chapter 3.

2.1.2 Relativistic Jets

Jet morphology

The most distinguishable features of a radio-loud AGN, the jets emitted from the core of the galaxy are the subject of much study - yet still comparatively little is known about them. High-resolution VLBI images have enabled their study on a sub-milliarcsecond scale, and a few salient properties about their behaviour and morphology have emerged.

The currently accepted AGN model envisions the jets as being produced in an antiparallel pair, shooting off in opposite directions perpendicularly to the disk. These have been observed in radio galaxies, where the jets are clearly visible and extend great distances from the core. However, many of the brighter quasars and blazars present as asymmetric sources with only one jet (one such example is the blazar 4C 21.35 studied in this report). This can be explained by the small angle at which the jet is observed, and relativistic beaming of the observed flux (see below). The jet is simply seen "head-on", and its brightness is such that its twin, propagating in the opposite direction, is simply invisible.

The jets are believed to originate in the core of the AGN, at the accretion disk, as stated above. The accelerated plasma (whose nature is still undetermined), moving at relativistic speeds, is emitted from a very small region, roughly $10 - 10^2 R_G$ (~ 0.01 parsec as seen in Junor et al. (1999) where $R_G = GM_{bh}/c^2$ is the gravitational radius of the central black hole, and a useful scale for AGN-related distances. The jet carries away angular momentum and energy from the accretion flow, and is accelerated and collimated up to about $10^3 R_G$ (Nakamura and Meier, 2009) although Vlahakis and Königl (2004) find that magnetic fields can accelerate and collimate the jets on parsec scales. It tends to become visible in the radio regime at this distance (still ≤ 1 pc). According to Lobanov (2010), after this "ultra-compact" stage at scales of ~ 1 pc, the jet passes through two more distinct regions where various physical mechanisms dominate its observed properties : parsec-scale flows (~ 10 pc scales) which are dominated by relativistic shocks, and large-scale jets (~ 100 pc) where the instability of the jet plasma starts to dominate its behaviour. The shocks and slowing down of the jet are due to collisions with the interstellar medium and diffuse gas surrounding the core and its host galaxy. This explains the presence of large radio lobes at the ends of jets as seen in active radio galaxies.

Synchrotron radiation

As the charged particles are accelerated and collimated by the powerful magnetic field in the accretion disk, they attain relativistic speeds, and are ejected from the core at an appreciable fraction of c . This is the cause of the synchrotron radiation responsible for the radio emissions of the quasar. It must be noted, however, that AGN synchrotron radiation is believed to cover the entire spectrum from radio to gamma-rays.

Synchrotron radiation is analogous to cyclotron radiation, in that particles accelerated by a magnetic field will radiate. However, synchrotron radiation is much more complex than cyclotron radiation, as it is defined when the particles are moving at relativistic speeds.

In general, a charged particle in an electromagnetic field will be subjected to the Lorentz force, given by :

$$\mathbf{F} = q [\mathbf{E} + \boldsymbol{\beta} \times \mathbf{B}], \quad (2.1)$$

where q is the charge on the particle, \mathbf{E} and \mathbf{B} are respectively the electric and magnetic fields, and $\boldsymbol{\beta} = \frac{\mathbf{v}}{c}$ with \mathbf{v} the velocity of the particle.

Considering the case where there is no electric field, the Lorentz force will cause the particle to spiral around the direction of the B-field, in a helical motion. This *gyration* will have an angular frequency given by

$$\omega_B = \frac{qB}{\gamma mc} \quad (2.2)$$

where γ is the familiar Lorentz factor, $\gamma = 1/\sqrt{1 - \beta^2}$ (all as given by Rybicki and Lightman (1979)).

The total emitted power of the accelerated particle can then be derived, and is shown to be :

$$P = \frac{4}{3}\sigma_T c \beta^2 \gamma^2 U_B. \quad (2.3)$$

Here, $\sigma_T = 8\pi q^2/3mc^2$ is the Thomson cross-section and $U_B = B^2/8\pi$ is the magnetic energy density. The derivation of this result is covered in detail in Rybicki and Lightman 1979.

Because the particles are moving at relativistic speeds towards the observer, an effect known as *relativistic beaming* occurs, by which the observed flux of the radiation is increased due to the Doppler effect and the effects of relativity. As the radiation reaches the observer, its frequency is Doppler shifted upwards, giving a higher-energy wave. At the same time, the source moving at relativistic speed is seen as being smaller in the observer's frame. This leads to a beaming effect whereby the received flux S_ν is amplified by the Doppler factor,

$$\delta = \frac{1}{\gamma(1 - \beta_{\parallel} \cos\Theta)} \quad (2.4)$$

β_{\parallel} is the velocity component in the direction of the observer and Θ is the angle of viewing. The amplification is generally of a factor D^3 or D^4 , but overall depends on the spectral index of the emission. In the scope of this report, where no comment is made about the source spectrum, it shall be assumed that $S_{\nu,\text{obs}} = \delta^4 S_{\nu,\text{em}}$.

The relativistic beaming of synchrotron emission plays a large part in the brightness of jets with a very small viewing angle.

Superluminal motion

So far, it has been assumed that the emitted jets travel at relativistic speeds, all the while avoiding the question as to why this is thought to be the case. This property can be derived from an intriguing phenomenon observed in the jets : *superluminal motion*. Indeed, when the first multi-epoch studies of jets using VLBI were undertaken, the transverse velocities of the jets were found to have values greater than c (Cohen et al., 1977). Evidently, if the theory of general relativity holds this is physically impossible - nothing can travel faster than the speed of light.

Such motion, however, was in fact predicted by British astronomer Martin Rees in 1966 for radio-emitting sources moving at relativistic velocities. The observed faster-than-light motion is due to an “optical effect” caused by the large relative speed with which two emitting parts of a jet are moving away from each other.

Indeed, if the angle of sight along the jet is small, and $\beta = \frac{v}{c}$ is close to 1, the observed speed v_{obs} will be larger than c . This is illustrated in figure 2.4 below:

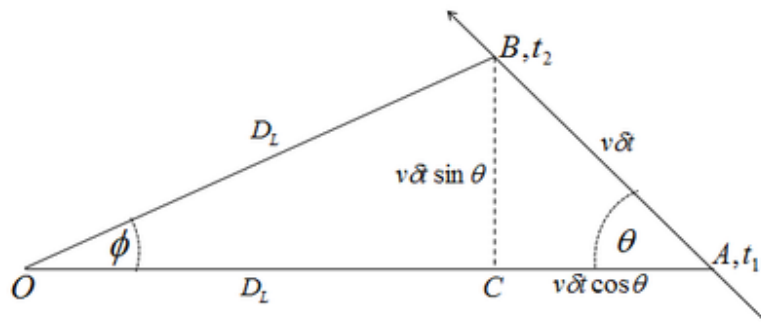


Figure 2.4: A geometrical illustration of superluminal motion : the emitting source starts at A and travels to B at an angle θ to the observer. The apparent transversal motion from C to B seems to occur with superluminal velocity.

At t_1 , the source is at A, and emits radiation which reaches observer O at time

$$\Delta t_1 = \frac{D_L + v\delta t \cos \theta}{c}. \quad (2.5)$$

The source reaches B after a time

$$t_2 - t_1 = \delta t,$$

and the resulting radiation reaches O at time

$$\Delta t_2 = \delta t + \frac{D_L}{c}. \quad (2.6)$$

The time between the observed positions, $\delta t' = \Delta t_2 - \Delta t_1$ is then given by :

$$\delta t' = \delta t - \frac{v\delta t \cos \theta}{c} = \delta t(1 - \beta \cos \theta). \quad (2.7)$$

Hence :

$$v_{obs} = \frac{BC}{\delta t'} = \frac{v\delta t \sin \theta}{\delta t(1 - v/c \cos \theta)} \quad (2.8)$$

$$\beta_{obs} = \frac{\beta \sin \theta}{1 - \beta \cos \theta}. \quad (2.9)$$

It can be seen from equation 2.9 that β_{obs} will be greater than 1 for small θ and β close to 1.

The observed motion from B to C in figure 2.4 is what is known as the *internal proper motion* of the source, and is defined as

$$\mu = \frac{\Delta\Theta}{\Delta t}, \quad (2.10)$$

where $\Delta\Theta$ is the angular distance a given source has travelled in time Δt (Falla and Floyd, 2002).

A distinction needs to be made, at this point, between two circumstances in which superluminal motion may arise. The first, and most straightforward, is when the source and the observer are in the same frame of reference. In this case, one can refer to the relativistic *motion* of the source, and the apparent faster-than- c velocity is simply due to the geometry of the observation and the finite speed of light. Equation 2.4 is, in this instance, valid for describing the jet at all speeds.

An example of such superluminal motion can be found in microquasar GRS 1915+105, which was the first superluminal source to be found in the Milky Way (Mirabel and Rodríguez, 1994). In this case, the source and observer are considered to be in the reference frame of the galaxy, and the distance to the source can be determined independently from spectral measurements. The observed velocity of the approaching jet is found to be $\sim 1.25c$, and the actual β was found to be $\sim 0.92c$ (again from Mirabel and Rodríguez, 1994). These results provided evidence for the nature of superluminal motion (being due to light travel time across an expanding source).

However, in the case of extragalactic sources exhibiting superluminal motion, equation 2.9 cannot directly be applied. Indeed, due to the expansion of the universe, the distance separating the source and the observer means that they are not in the same rest frame. The time Δt , as defined in equation 2.10, is affected by “cosmological time dilation”. Essentially, for an extragalactic, ‘cosmological’ source, the time interval Δt_{obs} as measured in the observer’s time frame is given by

$$\Delta t_{obs} = (1 + z)\Delta t \quad (2.11)$$

where the redshift z is given by $1 + z = f_{emitted}/f_{observed}$, in terms of the frequency of the source radiation.

Furthermore, a reliable determination of the distance of the source at intergalactic distances is only possible using redshift measurements. A common cosmological distance measure is the luminosity distance D_L - related to the flux of light received by the observer, it can be derived from cosmological parameters and the redshift. D_L can in turn be related to the angular-size distance D_a , which is the ratio between the linear size and angular size of the object, by

$$D_L = (1 + z)^2 D_a. \quad (2.12)$$

The transverse velocity v_{obs} , as defined in equation 2.8, is then given by

$$v_{\text{obs}} = \frac{\Delta\Theta}{\Delta t} D_a, \text{ in the source frame.} \quad (2.13)$$

Accounting for the effects of cosmological dilation (equation 2.11) leads to the expression

$$v_{\text{obs}} = (1 + z)\mu D_a = \mu D_L / (1 + z), \quad (2.14)$$

with μ measured in the observer's frame. The equivalent of equation 2.9 for a cosmological source can hence be written,

$$\beta_{\text{obs}} = (1 + z)\mu D_a \frac{1}{c} = \frac{\beta \sin \theta}{1 - \beta \cos \theta}. \quad (2.15)$$

It can be seen that for β close to 1, and for small θ , β_{obs} will be greater than one. Conversely, Falla and Floyd (2002) showed that if superluminal motion is observed, β is necessarily greater than $1/\sqrt{2}$, indicating a relativistic propagation velocity. Most, if not all jets in radio-loud quasars present superluminal motion (Lister et al., 2009), and it can be concluded that such speeds are characteristic of jets in AGNs.

Equation 2.15 will later be used to obtain the velocity and angle of sight for the jet studied in this report.

2.2 Interferometry and VLBI

The high-resolution study of extragalactic objects such as the Active Galactic Nucleus in this report has only been made possible thanks to the development of precise interferometry techniques. In this section, the fundamental concepts of radio interferometry are presented using the simple example of a two-element setup; following that the discussion will turn to the technique used for this project, VLBI (Very Long Baseline Interferometry), and the instrument used, VLBA (the Very Long Baseline Array). The discussion of these methods will be kept relatively brief, as more detailed explanations can be found, among others, in the textbooks by Burke and Graham-Smith (2002) and Thompson et al. (2001).

2.2.1 Interferometry : Fundamental Concepts

It is convenient to introduce the concept of radio interferometry using the simplified example of a two-antenna setup as shown in Figure 2.5.

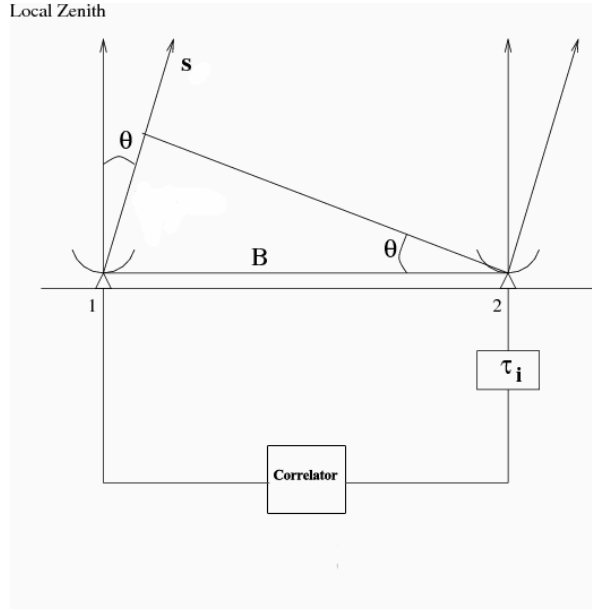


Figure 2.5: A simple two-element interferometer. The observed source is along the direction vector \mathbf{s} . The two antennas are separated by the baseline vector \mathbf{B} . The output signals are fed into a correlator, and it is possible to insert an artificial delay τ_i in the signal from antenna 2 to compensate for the later time of arrival of the radiation. *Source*: Bhatnagar, 2001.

The two antennas are separated by a baseline vector \mathbf{B} and are observing a radio source in the direction given by \mathbf{s} . This source is sufficiently far away that the radiation arriving at both antennas can be considered parallel. For simplicity, the source is considered to be a single point, emitting monochromatic radiation. With both antennas tracking the source, it emerges from simple geometry that the radiation arrives at antenna 1 with a delay

$$\tau_g = \frac{\mathbf{B} \cdot \mathbf{s}}{c} \quad (2.16)$$

with respect to antenna 2. This delay is known as the *geometric delay*. As can be seen on the figure, the antennas are set up so that it is possible to introduce an artificial, adjustable delay τ_i in the closer antenna. This will be of importance when sources having a finite spatial extent are considered.

The antennas each produce a response to the received signal according to the received frequency, ν , which can be written as a complex sinusoid: antennas 1 and 2 produce $V_1 \propto E e^{i2\pi\nu(t-\tau_g)}$ and $V_2 \propto E e^{i2\pi\nu t}$ respectively. These signals are then cross-correlated with each other, i.e., they are multiplied and the time average is taken.

This is useful for two reasons. Firstly, the cross-correlation has dimensions of power, and thus can be related to antenna area $A(\mathbf{s})$ and source flux S (and is then called

cross-power product). Second, the cross-correlation permits easy filtering out of higher frequencies corresponding to signal terms not entirely dependent on τ_g which then gives a final correlator output of :

$$R_{v_1 v_2} = A(\mathbf{s})S \cos(2\pi\nu\tau_g). \quad (2.17)$$

As seen in equation 2.16, the geometric delay is related to the source direction. This varies as the earth rotates, and it is this directional variation that causes the appearance of sinusoidal fringe variation.

However, this initial derivation is based on a point source, monochromatic model. To be able to apply this to real sources which have finite size and emit over a range of different frequencies, some modifications must be made. Interferometers also have finite bandwidth, and this introduces effects which must equally be taken into account.

In practice, it is useful to work in the frequency domain when analysing interferometer output, and the most commonly-used quantity is simply the Fourier transform of the cross-power product (Equation 2.17), known as the cross-spectrum power density,

$$S_{v_1 v_2}(\nu) = A(\mathbf{s})S \exp(i2\pi\nu\tau_g). \quad (2.18)$$

The effect of finite receiver bandwidth is to create an interferometer response function or *delay beam* which will restrain the number and shape of visible fringes.

Assuming that the radio spectrum of a source changes slowly with frequency, and that the bandwidth is only a small fraction of the studied spectrum, the spectrum within the band can be considered flat. Using this approximation, the cross-spectrum power density is then found by integrating the single-frequency response over the bandwidth $\Delta\nu$. For the example of a simple square bandpass centered in ν_0 , this can be expressed as :

$$\langle S_{v_1 v_2}(\nu) \rangle = \int_{\nu_0 - \Delta\nu/2}^{\nu_0 + \Delta\nu/2} S_{v_1 v_2}(\nu) d\nu \quad (2.19)$$

which gives :

$$S_{v_1 v_2}(\tau_g) = \Delta\nu A(\nu_0, \mathbf{s})S(\nu_0) \exp(i2\pi\nu\tau_g) \text{sinc}(\Delta\nu\tau_g), \quad (2.20)$$

where the delay beam is seen to be the sinc term in Equation 2.20.

Additionally, as mentioned above, observed sources always have a certain, finite extent. To take this into account, the source direction \mathbf{s} must now be written as

$$\mathbf{s} = \mathbf{s}_0 + \sigma, \quad (2.21)$$

where \mathbf{s}_0 is a position vector (generally directed towards the center of the source or *phase tracking centre*) and σ is a small vector, normal to \mathbf{s}_0 that describes the extent of the source. It is now that the instrumental time delay τ_i mentioned earlier comes into the picture. By setting $\tau_i = \tau_{g0}$, the geometrical delay is cancelled out and the only remaining delay between the signals is related to size of the source :

$$\tau = \tau_g - \tau_i = \frac{\mathbf{B} \cdot (\mathbf{s}_0 + \sigma)}{c} - \tau_i. \quad (2.22)$$

Taking the example of a small element of an extended source subtending a solid angle $d^2\Omega$, we can then rewrite expression 2.20, replacing the flux with the specific intensity, or brightness, B_ν (flux per angles per Hertz) and including the delay beam terms in the expression for the effective area $A(\mathbf{s})$:

$$S_{v_1 v_2}(\nu_0, \mathbf{s}_0 + \sigma) = \Delta\nu A(\mathbf{s}_0 + \sigma) B_\nu(\mathbf{s}_0 + \sigma) \exp[i2\pi\nu(\tau_g - \tau_i)] d^2\Omega. \quad (2.23)$$

This can be expressed in a more simple manner if a couple of approximations are made: firstly, the total source size is presumed to be small compared to the delay beam; second, the spectrum of the source is constant across the bandpass . This means that any delay beam effects are insignificant, and that the signal can be approximated using the centre frequency of the bandpass. Integrating expression 2.23 over the entire source yields :

$$S_{v_1 v_2}(\mathbf{s}_0) = \int_{4\pi} A_{rel}(\sigma) B_\nu(\sigma) \exp\{i2\pi[\mathbf{b}_\lambda \cdot (\mathbf{s}_0 + \sigma) - \nu\tau_i]\} d^2\Omega. \quad (2.24)$$

This expression uses the approximations stated above to remove the effects of the delay beam and let ν be the centre frequency specifically, thus suppressing the bandwidth term $\Delta\nu$. Furthermore, the relative antenna area A_{rel} , with value unity in the direction \mathbf{s}_0 , is used because it depends solely on σ ; the geometric time delay is expressed explicitly in terms of the direction vectors, with \mathbf{B} , the baseline vector, expressed in dimensionless units: $b_\lambda = \mathbf{B}/\lambda$.

This expression is of great importance, because it can be used to define a new quantity relating the output of the interferometer with the actual source brightness. This is called the *complex visibility*. Considering, in equation 2.24, that the instrumental delay is set to cancel out the geometric delay, the complex visibility V can be written:

$$V = \int A_{rel}(\sigma) B_\nu(\sigma) \exp(i2\pi\mathbf{b}_\lambda \cdot \sigma) d^2\Omega. \quad (2.25)$$

This is a key equation in interferometry, and it can be seen that the complex visibility is related to the Fourier transform of the source brightness. In order to study the source, it is therefore necessary to find a way to extract the brightness from the actual observable, the correlator output.

The complex visibility is usually represented in what is known as the (u, v, w) coordinate system, which defines the u, v plane as the plane containing the baselines, and w as the source direction. This is a rectilinear coordinate system, with u projected east and v projected north as seen in figure 2.6. By convention, the offset vector σ is considered to be parallel to the u, v plane and has coordinates x and y as shown in figure 2.6.

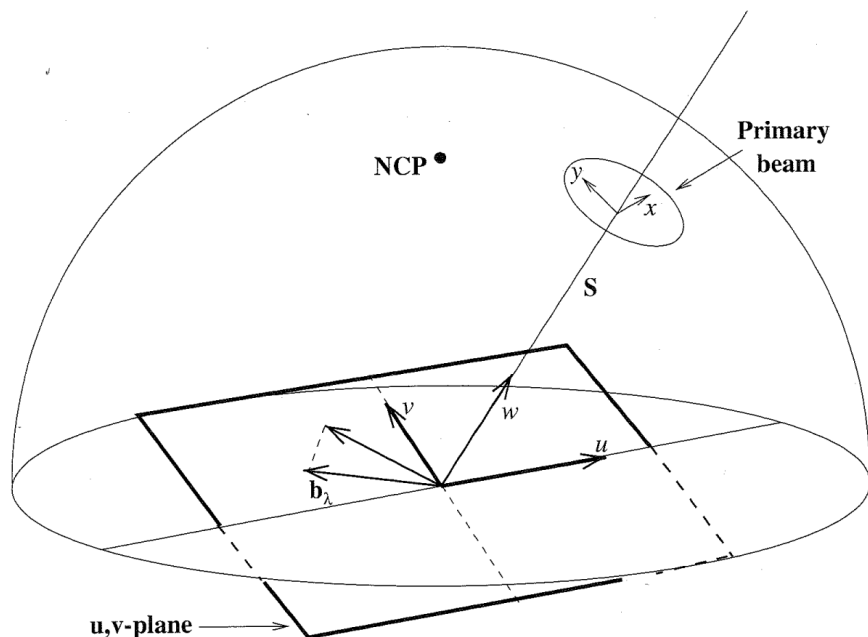


Figure 2.6: Geometrical layout of the u, v plane showing an extended source. x and y are the components of the offset σ , \mathbf{b}_λ shows a possible baseline and NCP represents the North Celestial Pole. Taken from Burke and Graham-Smith (2002).

If equation 2.25 is expressed using direction cosines, and the small-angle approximation is then taken (valid when, as before, the source size is assumed to be small compared to the beam), the complex visibility can then be written in terms of u, v, x and y :

$$V(u, v) \approx \int A(x, y) B(x, y) e^{i2\pi(ux+vy)} dx dy \quad (2.26)$$

As seen before, the complex visibility is essentially the Fourier transform of the source brightness for a given point in the u, v plane. This point is simply the projection of the relevant baseline vector in the u, v plane. Hence one interferometer observation, with a

given baseline, will yield a single element of the source brightness distribution. However, it must be noted that the brightness $I^D(x, y)$ given by the inverse transform of the visibility is in fact the convolution of the actual brightness $B(x, y)$ with the antenna response function or beam pattern $A(x, y)$, as given in equation 2.27

$$I^D(x, y) = A(x, y) \otimes B(x, y) = \int_{-\infty}^{+\infty} \int_{-\infty}^{+\infty} V(u, v) e^{-i2\pi(ux+vy)} du dv \quad (2.27)$$

In order to build up a picture of the entire source, it is necessary to "sample" the u, v plane at as many points as possible and obtain the Fourier transform of the whole source brightness distribution. Inverting this will then give the actual distribution. Therefore, in order to construct a complete picture of a given source using interferometry, many baselines are needed. This realisation led to the development of many-telescope arrays and *aperture synthesis*, which are explored in the next section.

2.2.2 Aperture Synthesis

The observation of an extended radio source using interferometry, as has just been shown, requires an extensive sampling of the u, v plane in order to obtain a complete image of the brightness distribution. The use of a series of baselines in order to do this is called aperture synthesis. This can be achieved using interferometer arrays comprising many different telescopes, and taking advantage of the earth's rotation to obtain a wide "spread" of continuous coverage in the u, v plane. The latter technique is known as *Earth-rotation synthesis*.

Recalling the relationship between aperture diameter and angular resolution, $\theta \simeq 1.22 \frac{\lambda}{D}$, where λ is the wavelength of the radiation considered and D the diameter of the aperture, it is possible to obtain extremely high resolutions using interferometers as D is replaced by the longest baseline length.

A wide spacing between antennas is therefore desirable, however this puts practical limits on the number of intermediary spacings that can be used to provide continuous coverage of the u, v plane. An example of u, v coverage can be seen in Figure 2.7, for one of the observations of quasar 1222+216 used in this report.

According to the Nyquist sampling theorem, a discrete Fourier transform can faithfully reconstruct a continuous function if the sampling rate is at least twice the bandwidth limit. Applying those criteria to this case, the spatial sampling rate should be at least twice as high as the highest spatial frequency (i.e longest baseline) of the interferometer array.

The treatment of data obtained via aperture synthesis is a complex process, and involves extracting the brightness distribution of the source from the visibility data using Fourier transforms and deconvolutions. These processes are treated in detail in Chapter 4 of this report.

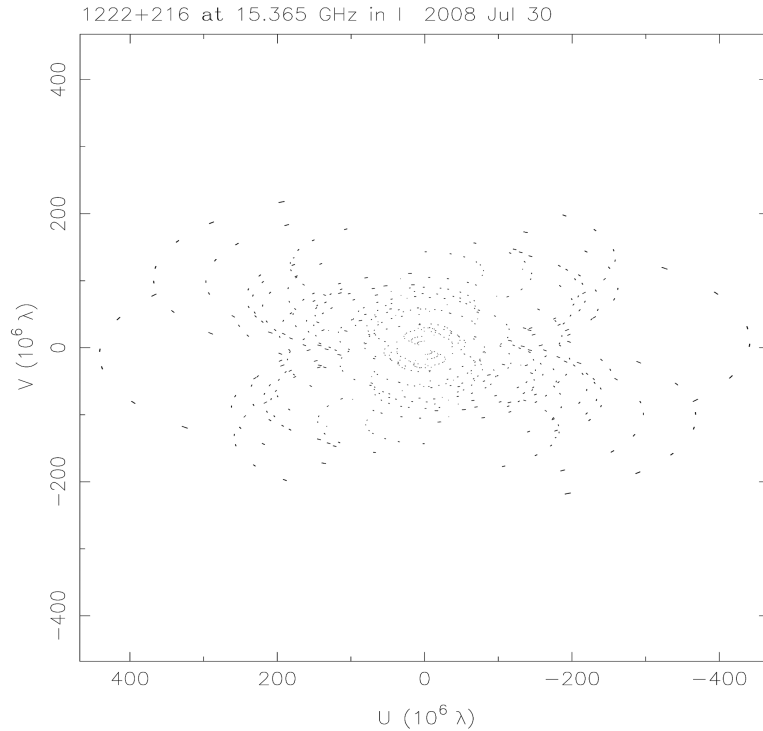


Figure 2.7: U,V plane coverage for an observation made by the Very Long Baseline Array, using 45 distinct baselines over 185 minutes (3 hours 5 minutes). Image made using raw visibility data and DIFMAP.

The antenna arrays used in modern radio astronomy can either be regrouped within a relatively small area (such as the Very Large Array in the United States), or spread across an entire continent (such as the Very Long Baseline Array (VLBA), used in this project and detailed in the next section). Provided the signals are properly correlated, there is no inherent limit to baseline length and interferometers with elements in space have already been used (Levy *et al.*, 1986). The latter type of array, in which antennas are too far apart to be "hard-wired" between themselves, is known as a Very Long Baseline Interferometry (VLBI) apparatus. VLBI is described in the next section.

2.2.3 Very Long Baseline Interferometry and the VLBA

The observations of the source 1222+216 used in this report were made by the North American telescope array known as the VLBA. Comprised of ten telescopes spread across the United States and operated by the National Radio Astronomy Observatory (NRAO), it has been operational since 1993, when the final telescope in Mauna Kea (Hawaii) was completed (Napier, 1995). The positions of the various telescopes are illustrated in Figure 2.8. The longest baseline is between the telescope in Mauna Kea and the one

in St.Croix, in the Virgin Islands, with a length of 8611 km (Romney, 2011). The ten telescopes provide $N(N - 1)/2 = 45$ baselines for a u,v-plane coverage as seen in Figure 2.7.

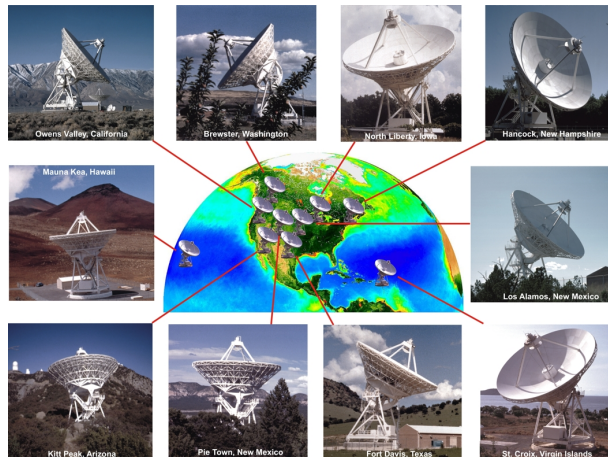


Figure 2.8: An illustration of the 10 telescopes comprising the VLBA, and their locations.(Image courtesy NRAO)

The telescopes are not connected between themselves due to the prohibitive distances involved, instead the signals are recorded digitally on redundant hard drives along with synchronization signals linked to the oscillations of an ultra-stable hydrogen maser located at each station.

Once recorded, the signals are sent to the central correlator in Socorro, New Mexico, and undergo a calibration and correlation process which yields the final complex visibility as described in section 2.1.1.

2.3 Object of study : 4C+21.35

Having dealt with the theoretical background regarding AGNs and Radio Interferometry, now would be an appropriate time to delve into the specifics of the source studied in this report: radio source 4C+21.35, also known as 1222+216 (in B1950 coordinates) or 1224+2122 (in J2000).

The source forms part of the MOJAVE project (Monitoring of Jets in Active galactic nuclei with VLBA Experiments) sample, and is also part of the samples monitored by the Fermi Large Area Telescope, which detects gamma-rays. Criteria for selection as part of the MOJAVE source list can be found in Lister et al. (2009).

Classified as a bright, flat-spectrum radio source (Healey et al., 2007), due to a flux density of around 1000 mJy at an observation wavelength of 8.4 GHz, 4C+21.35 is

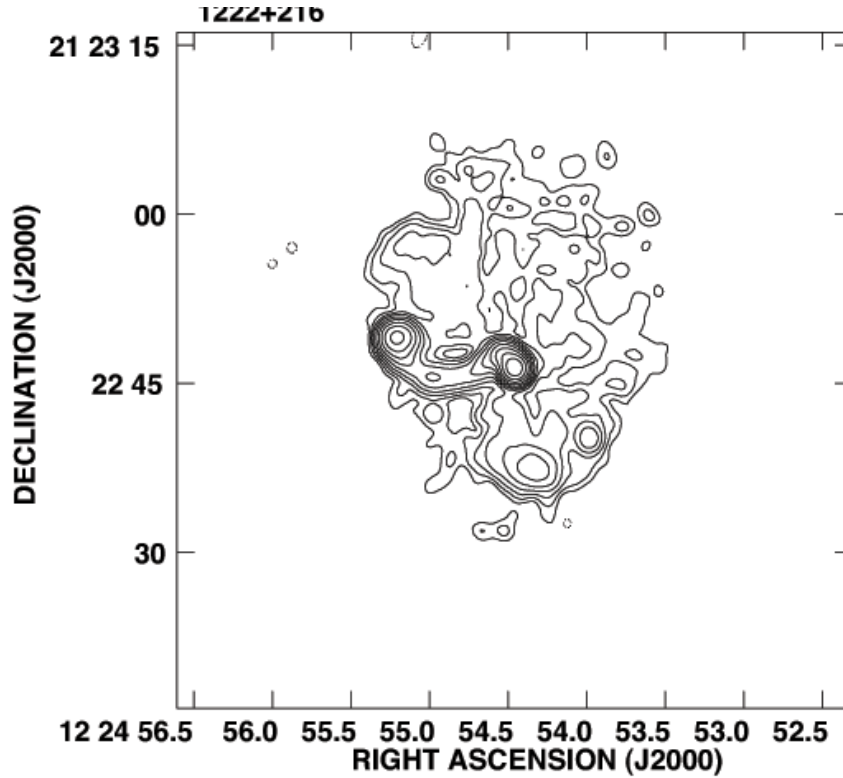


Figure 2.9: A 1.4 GHz image of 4C+21.35. The source is seen to be centered on a bright core component, with a collimated emission to the left of this, and a “halo” of emission giving an overall round shape. Image from Cooper et al. (2007).

effectively a quasar. It has a redshift of $z = 0.432^1$, corresponding to a luminosity distance of 2367 Mpc¹ and an angular-size distance of 5.60 pc/mas¹.

Images made using VLBI at 1.4 GHz (Cooper et al., 2007) show the source to present emission on two sides around an unresolved core component (Figure 2.9). Higher frequency imaging done by the MOJAVE team² at 15.3 GHz and the Boston University Blazar Monitoring project³ at 43 GHz show this core component to be a one-sided, parsec scale jet (with an angular width of about 1 mas). The compact and bright jet points to 4C+21.35 being a blazar.

A look at the Spectral Energy Distribution (SED) of the source (Figure 2.10) can help to confirm this. As mentioned in section 2.1.1, blazars do not possess any emission lines in their spectra, which seems to be the case. Furthermore, the SED presents the “double

¹Data taken from the MOJAVE database, <http://www.physics.purdue.edu/MOJAVE/sourcepages/1222+216.shtml>, where the cosmology assumed in calculations is $H_0 = 71$ km/s/Mpc, $\Omega_\lambda = 0.73$ and $\Omega_m = 0.27$.

²<http://www.physics.purdue.edu/MOJAVE/sourcepages/1222+216.shtml>

³http://www.bu.edu/blazars/VLBA_GLAST/1222.html

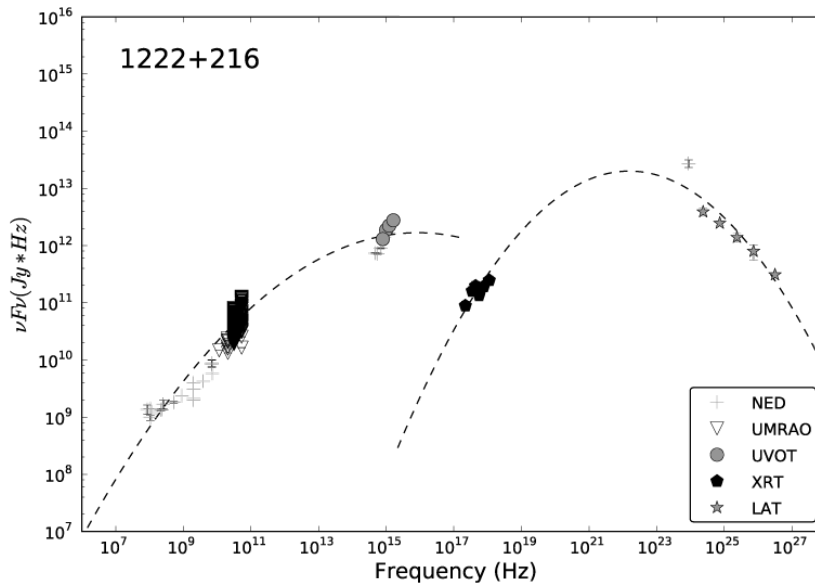


Figure 2.10: The SED for 4C+21.35, from Chang, 2010. The data points are taken from various observations across the electromagnetic spectrum: radio(NASA Extragalactic Database, University of Michigan Radio Astronomy Observatory), UV and optical (UVOT telescope on the Swift satellite), X-ray (XRT on the Swift satellite) and γ -ray (Fermi Large Area Telescope). The most obvious features of the SED are the peaks in the optical and soft gamma regions, identifying the object as a blazar.

bump” characteristic of blazars, as presented in Fossati et al., 1998, where the author shows that blazar spectra present two peaks, one in the radio/optical domain due to synchrotron emission, and one in the γ -ray.

It can therefore be seen that blazars emit strongly in the γ -ray domain of the EM spectrum. Indeed, it has recently been suggested that there is a link between jet behaviour and gamma ray emission in radio-loud AGNs : Lister et al. (2009) find a connection between higher velocities and brighter objects, while Pushkarev et al. (2009) find a link between jet opening angles, line of sight angles, and brightness. This correlation motivated the search for a feasible object of study for this report : the presence of γ -ray activity in an AGN would indicate a jet propagating at relativistic speeds. 4C+21.35 was chosen as one of the MOJAVE sources having recent, very energetic (photon energy $> 100\text{MeV}$) γ -ray flares reported by the Fermi-LAT telescope: one in April 2009⁴, one in December 2009⁵, and one in April 2010⁶. In each case the peak flux was higher than the last, which indicates a steady rise in emission levels. A further flare was reported just before submission of this report, on June 19th⁷, where the flux had further risen over its peak April 2010 value, thus confirming the upward trend.

⁴<http://www.astronomerstelegam.org/?read=2021>

⁵<http://www.astronomerstelegam.org/?read=2349>

⁶<http://www.astronomerstelegam.org/?read=2584>

⁷<http://www.astronomerstelegam.org/?read=2687>

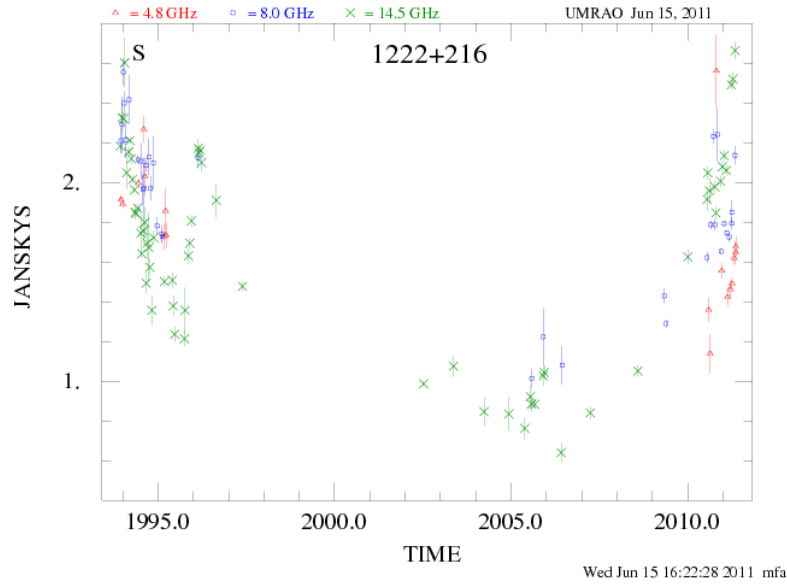


Figure 2.11: Light curve for 4C+21.35 at 4.8, 8.0, and 14.5 GHz of the blazar 4C+21.35(1222+216). Image used with kind permission from Margo Aller and the University of Michigan Radio Astronomy Observatory.

Interestingly, the flares occurred along the same time period as a sharp increase in radio flux (the period in this report) as seen in Figure 2.11. The light curve covers three different frequencies as opposed to the single one used in this project; it can be seen that there is a general increase over the entire radio spectrum. Flux evolution based on data treatment in this report can be seen for comparison in Figure 4.7.

The VLBA data provided online by the MOJAVE group was then downloaded and processed as described in chapter 3, so as to study the jet. There were eight data samples from different dates (or epochs) available from 2008 to 2010. It was decided to stick to the data samples available since the launch of the Fermi-LAT telescope, given that the γ -ray observations from said telescope were used in determining interesting sources. These are detailed in the next chapter. The analysis of jet kinematics (i.e. deriving velocities) was of particular interest, as this had been undertaken for previous epochs by Lister et al., 2009 and as such was available for comparison. Comparison and further analysis of the results are presented in chapter 4.

Chapter 3

Imaging and data treatment

The blazar 4C+21.35 has so far been observed 9 times at 15 GHz using the VLBA since the launch of the Fermi-LAT space telescope in 2008. The observations were made as part of a routine coverage of the MOJAVE sample, which focuses on taking regular VLBI images of active radio jets in AGNs. The different dates of observations, or epochs, are listed in Table 3.1 below. All these observations were made at a frequency of 15.3 GHz, corresponding to ~ 2 cm wavelength. According to the VLBA observational status summary, this corresponds to an angular resolution of 0.5 mas^1 , which for an angular-size distance of 5.60 pc/mas would give an image of the jet on the scale of a few parsecs.

Epoch	Date
1	30/07/2008
2	28/05/2009
3	27/10/2009
4	26/12/2009
5	12/07/2010
6	29/09/2010
7	13/11/2010
8	24/12/2010

Table 3.1: The 9 different epochs at which the observations used in this report were made. These were all pre-scheduled observations in the scope of regular MOJAVE monitoring of selected bright radio jets.

¹<http://www.vlba.nrao.edu/astro/obstatus/current/>

3.1 Data reduction

The raw data received from the VLBA correlator needs to be processed using various techniques to be able to extract the final brightness data and make a faithful image of the source. There are two main steps : calibration and “cleaning”. The data, in this case, was calibrated by the MOJAVE team as detailed in Lister et al. (2009). The resulting visibility data are available from the MOJAVE website² and were used as a starting point for the cleaning process. The data cleaning and production of images was then performed by myself, using the program DIFMAP (Shepherd, 1997) and the AUTOMAP script written by Taylor (1997). It should be noted that each epoch is processed separately, as the techniques involved must be applied specifically to each set of visibilities. What follows in this section is more of a theoretical overview of the procedures involved, as the details behind the various algorithms used are highly technical and beyond the scope of this report.

3.1.1 Calibration

Before it is possible to derive any image data from the complex visibilities, they need to be calibrated. Indeed, instrumental and observational factors can affect the results, and these must be compensated for. This is known as *a-priori* calibration. This is done using the standard program AIPS (Astronomical Image Processing System). While the specifics of *a-priori* calibration will vary depending on the source sample, telescope array used and numerous other factors, the basic steps remain the same. These are outlined here, along with the implementations of these steps by the MOJAVE team (Lister et al., 2009)

Pre-calibration data flagging First of all it is important to get any “bad” data points, due to external factors (inclement weather, for example) or recording problems at single antennae. Lister et al. looked for excessively high system temperatures as an indicator of bad weather conditions to flag out the corresponding data points.

Amplitude calibration The resulting visibilities then have to be amplitude-calibrated due to instrumental effects. Due to the correlation, as mentioned in section 2.2, there is very little noise in the signal itself, but the effect of antenna gain, atmosphere opacity effects (there will be some absorption as a function of the zenith angle, as described in Thompson et al. 2001 and amplitude loss due to digitalization of the signal all have to be corrected for. The standard method for this (used in the MOJAVE paper) is using the antenna gain curves and system temperatures, while observing a known source, to calibrate the amplitude.

Phase calibration It is also necessary to calibrate the visibility phases. These are

²<http://www.physics.purdue.edu/astro/MOJAVE/sourcepages/1222+216.shtml>

affected by instrumental offsets and phase gradients occurring in the various frequency channels of the observation (the total bandwidth is separated into channels, known as IFs, so as not to have to deal with the entire bandwidth in one go). Caused by the path the signal takes during the recording and correlation, these offsets can be corrected using the "phase-cal" signal, which is a regular pulse emitted during the recording and injected into the data. The phases in the studied samples were aligned using this method.

Fringe fitting Finally, some residual phase delays may remain, although this time due to differences between IFs. This is generally due to propagation effects in the atmosphere or inaccurate modeling of the interferometer. These are removed by fringe fitting (see Thompson et al., 2001, p.195). In the case of the MOJAVE samples, global fringe-fitting was not deemed necessary, because the sources were strong and compact, and the interferometer geometry was very well-known.

The visibilities were then phase self-calibrated (i.e. a model of the source is constructed and the differences between the model phases and observed phases are minimized) before being processed in DIFMAP.

3.1.2 "Cleaning" and image production

The calibrated visibilities represent the quantity $V(u, v)$ seen in equation 2.27. It is now finally possible to start extracting the brightness of the source, so as to construct a map of it. The basic process that needs to be performed is a discrete inverse Fourier transform of $V(u, v)$, followed by a deconvolution of the the true brightness $B(x, y)$ from the antenna response $A(x, y)$. A couple of commonly-used terms should be introduced here : $I^D(x, y)$, the inverse transform of the visibility, is know as the "Dirty Map", and $A(x, y)$ is known as the synthesis beam or "dirty beam".

Deconvolution and the clean algorithm

It is known from Fourier analysis that the convolution of two functions is equal to the product of the Fourier transforms of these functions. In equation 2.27, the lhs convolution is equal to the FT of the visibility times the *sampling function*, $S(u, v)$, which is simply a measure of how complete the u,v-coverage of the interferometer is. If the entire u,v-plane was continously sampled, the sampling function would be a constant, and the resulting dirty beam would simply be a delta-function, and determining the brightness would be trivial. However, the u,v-plane is never fully sampled, and deconvolution algorithms must try to account for the *un*-sampled areas. These un-sampled areas are responsible for unwanted local maxima in the dirty map, known as "sidelobes" which the algorithm will attempt to get rid of.

The deconvolution algorithm used by DIFMAP is called CLEAN (Högbom, 1974). The key underlying principle of the CLEAN algorithm is that it assumes the visibility map to

be empty overall, save for a few very bright points representing the source (this seems logical enough, taking into account the sensitivity of modern telescopes and the low amount of noise in the correlated radio output).

The basic *modus operandi* of CLEAN is as follows : within a given area of the dirty map (called a clean window), the algorithm will look for the brightest point and then subtract a given fraction of the dirty beam from the dirty map, at that maximum. The subtracted beam is known as a clean component, and the fraction is called the loop gain. What is left of the dirty map is then called the residual map. The clean component is effectively a delta function, with amplitude and position proportional to the maximum it was subtracted from. Both the clean component and residual map are stored, and the process is repeated with the new maximum in the residual map. This process is iterated until the highest residual maximum is below the average noise level.

At this point, the stored map containing all the clean components is then convolved with an ideal dirty beam : a pure gaussian with the FWHM of the original dirty beam. This “clean map”, added to the residual map, generally reproduces the brightness distribution quite satisfactorily.

The imaging process and automap

Having outlined the way the CLEAN algorithm works, it is fairly straightforward to describe the workings of DIFMAP. The visibilities take the form of a u,v FITS file which is read into DIFMAP. As in AIPS, any remaining “bad” data points can be edited out before the data processing begins; there are many different viewing modes available to help locate possible discrepancies.

Once the data is deemed satisfactory, the map parameters are set. Map size and pixel size will define the resolution of the final, clean map, but there are certain constraints: the map must be big enough to display the entire source (at least twice the size of the primary beam) and the pixel size must be less than half of the dirty beam FWHM. The weighting is then chosen, which defines how much weight is given to each baseline during the Fourier transform and CLEAN process. One can distinguish natural weighting, meaning that each baseline has equal weight, and uniform weighting. Natural weighting will produce a larger, more sensitive beam but lower resolution than uniform weighting, which gives more weight to baselines with higher spatial frequency (closer together). The mapsize for this report was taken to be 2048×2048 pixels (a side can only be defined as a power of 2), and the pixel size 0.05 mas/pixel. This gave a large map with a high resolution and detailed image of the source; furthermore, trial maps at 1024 pixels proved to cut off some of the jet.

With these parameters set, the CLEANing can begin. The CLEAN windows can be traced manually by the user, but in practice this is a lengthy process, and the script AUTOMAP, written by Pearson et al. (1994) for the purposes of automating the mapping process in the Caltech-Jodrell Bank surveys CJ1 and CJ2, was used. AUTOMAP produces satisfac-

tory maps when given well-calibrated visibility data, as was the case with the MOJAVE samples. It firstly self-calibrates the data with a point-source model, then produces a dirty map (by Fourier inversion, given by the command `mapplot`). The peak brightness is identified, and a window is drawn around it (1.8 times the size of the dirty beam FWHM). The area in the window is then CLEANed with a loop gain of 0.015 for 100 iterations, and the map is self-calibrated at every cycle (the phase differences between the model source and actual data are minimized, on a given time scale - the selfcal time starts off relatively small, and as the model improves is made larger and larger). This cycle is repeated until the residual map does not present any more peaks above 6 times the RMS flux of the map. This is done with uniform weighting. The process is repeated with natural weighting (and a larger window size) which is more sensitive to components that the uniform weighting clean wouldn't have picked up. The weighting was then biased towards longer baselines using a gaussian taper to pick up any remaining components. Finally the map is amplitude self-calibrated and then CLEANed again with 200 iterations and a lower threshold.

Due to the high quality of the *a priori* amplitude calibrations the data had already undergone, as well as the high brightness of the sources, it was deemed unnecessary to perform the mapping by hand (even though all the AUTOMAP parameters were inspected and set up to produce good results after a few trial runs). Indeed, "blind" mapping of a bright source is good enough to monitor the gross details of the source morphology, and perform a parametrization of the physical properties of the emitting features of the source using MODELFITting, as described below.

AUTOMAP, run with similar parameters by Xu et al. (1995) was found to generate maps with few to no errors compared to interactively-generated maps in 95% of cases. Upon inspection of the produced maps, and comparison with the existing MOJAVE maps, these were taken as satisfactory images. The maps of the source at all 8 epochs can be seen in chapter 4, Figure 4.2.

3.2 Modelfitting

Once the final brightness maps are obtained, they give useful insights into the aspect and general morphology of the source. However, in order to qualitatively study the jet, further image treatment is needed.

The VLBI data processing removes any absolute position information from the source image, however information on the flux density at various points on the map can be retrieved. In the context of this report, the main goal is to study the kinematics of the jet emitted by the blazar: determine its velocity and thus deduce the angle of viewing. In order to build up a reliable picture of the source that can be studied over the different epochs, it is necessary to fit a model to it. This can be achieved using the MODELFIT command in difmap. More information on the concept of model fitting in VLBI imaging

can be found, amongst others, in Pearson (1995).

The basic principle behind MODELFITTING is to fit a gaussian model component onto distinguishable features of the source. This amounts to identifying the brightest areas in the emission map and manually adding a component to the model. Once the source is fully modelled, it is possible to identify the same component in various epochs and thus track its evolution.

MODELFITTING is an iterative process. To begin with, a new dirty map is made from the CLEANED visibility map. Then, the brightest feature of the dirty map is located, and a model component (of size and shape determined by the user) is placed on the feature, “covering” it. This gaussian component will have a number of attributes corresponding to the feature it models : flux density, FWHM, and position.

Once it is in place, the `modelfit` command is run. This algorithm attempts to minimise the variations between the data and the model by fitting the parameters of the component to those of the actual visibilities. This is done using a least-squares fit, and the goodness of the fit is quantified using the value of reduced χ^2 (the sum of the squared differences between model and data divided by the number of degrees of freedom). The algorithm will run for a set number of iterations defined by the user, specifying the χ^2 each time.

In this case, circular gaussian components were used, so 4 parameters were allowed to vary : flux, 2 position coordinates, and component diameter. Despite not having the variability of elliptical components (over both axes) circular model components were chosen over elliptical ones because they enable easier identification of components across epochs and will not “collapse” like ellipses fitted to regions of high flux (this happens when an elliptical component’s minor axis goes to 0 when fitted to high emission areas).

Once the iterations are completed, the component is subtracted from the dirty map and a new residual map is created, and possible additional components are fitted. This is repeated until a satisfactory χ^2 value is attained, around $\chi^2 \leq 1$, and the residual map is smooth and featureless.

While the χ^2 value must be attentively monitored during the entire MODELFIT process, it is important to check the validity of the model in other ways. As mentioned above, DIFMAP comes with a number of different ways to visualize visibility data, these can also show the model components for comparison, thus aiding evaluation of the fit. Most useful are the `radplot`, `projplot` and `vplot` tasks, which plot the baseline amplitude as a function of its radius, visibility amplitude along a projected direction in the u,v-plane and amplitude and phase versus time respectively. For the data used in this project, no significant deviations in the model were found, and χ^2 reached a satisfactory value of around 0.9 for each map (see chapter 4 for all component details).

An important aspect of the MODELFIT process in this case was the desire to be able to identify components across the different epochs. To this end, the MODELFITTING was somewhat simplified by using the model of the previous epoch as a starting point

for the modelling of the next one. This was a useful and time-saving approach which enabled quick identification of components, as well as making it easy to distinguish the apparition of new components over time. Care must equally be taken not to add too many components, as for a complex model it is more difficult to identify components. When finally plotting component positions, the core (brightest) component was always taken as the origin to aid identification.

Determining the number of components that accurately described the map was largely a trial-and-error process, and initial models sometimes had more than 15 components. However, inspiration was taken from the previous work by Lister et al. (2009), where the source had been described with 8 components for the epochs leading up to the present sample epochs. Using this number as a guide, certain components were removed, and some refitted, to get a simpler model. All of this was done step-by-step while keeping a close eye on the goodness-of fit given by χ^2 and the various plots. There were also other, visual indicators as to the accurateness of a model: for example, if a removed component was indispensable to the model the program would “complain” by increasing another component to an implausible size to make up for it.

The final models contained either 8 or 9 components, as seen in Figure 4.2: 8 components for the first 2 epochs, and 9 for the rest. This indicated the apparition of a component, which would have been expected from the recent flaring activity. Plotting the component positions on top of the brightness maps shows a distribution consistent with the maps: 3 or 4 components can be found close to the core, a further 4 can be found in a bright area about 6-7 mas radially outwards, and a final component can be found in a feature about 15 mas from the core. A more detailed treatment of the component evolution is found in chapter 4.

Treatment of uncertainties

With the source brightness maps established, and the main features of the source described by mode components, it is possible to begin a quantitative analysis of the parsec-scale jet.

Chapter 4

Results and Analysis

The results of the mapping and model fitting described in the previous chapter will be presented here. The obtained component data will then be analysed across the different epochs and a kinematic analysis, determining the velocities β_{obs} of each component, will be carried out. This will in turn enable a calculation of the viewing angle θ of the source. These results will then be compared to those of (Lister et al., 2009), obtained for previous epochs, to see if my model is coherent with past analysis and if continuity can be established. Combined with a description of the flux evolution of the components, a qualitative picture of the jet behaviour can be built up and possible future behaviour can be conjectured.

4.1 Brightness maps

4C+21.35 was mapped according to the procedure described in section 3.1 for all 8 epochs, and these maps can be seen in Figure 4.2. The maps are centered on the brightest (core) component, and contour levels delimit the regions of flux in multiples of 1 mJy/beam (this contour level was chosen to give appropriate sensitivity and to distinguish the most possible features without showing noise on the map). Contour levels and peak flux are shown in Table 4.1. The source is seen to be a one-sided jet, expanding along a northward direction in relative declination. The unresolved core is roughly 1 mas long and 0.5 mas wide, and there is a second visible bright element, initially centered about 7 mas from the core and which moves progressively northward with time, seemingly “detaching” itself from the core. The area between the core and the second bright spot is very thin and collimated. Finally there is an additional emitting element, of quite low intensity (visually, from the contour levels, ~ 1.6 mJy).

While these maps give us a good indication of what the source looks like, due to the imprecisions inherent to the contours and the difficulty of identifying components visually it is necessary to fit model components to the maps. This is possible because the

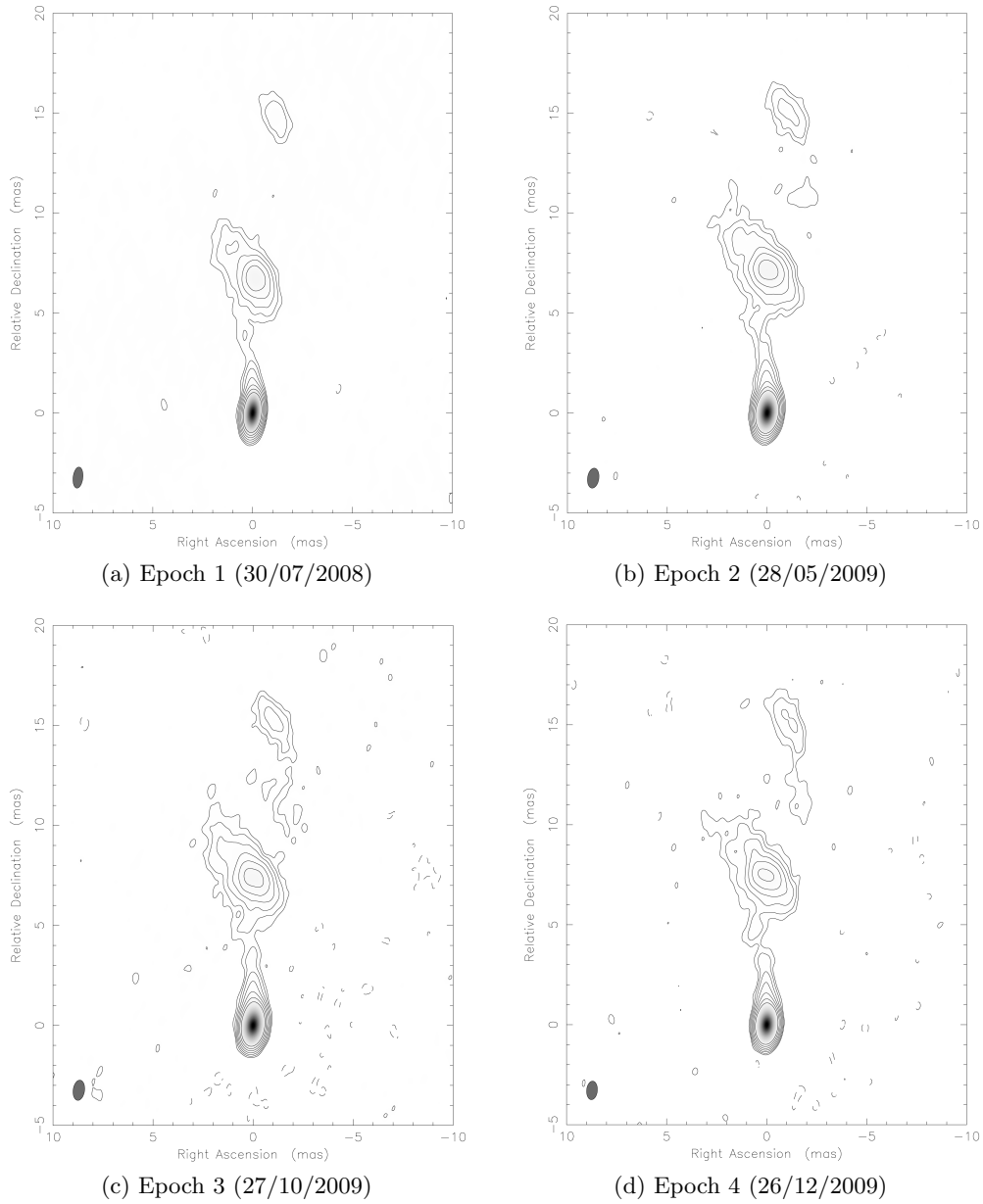


Figure 4.1: The brightness distribution maps for 4C+21.35 over the 8 studied epochs. See Table 4.1 for information about flux, beam size and contour levels.

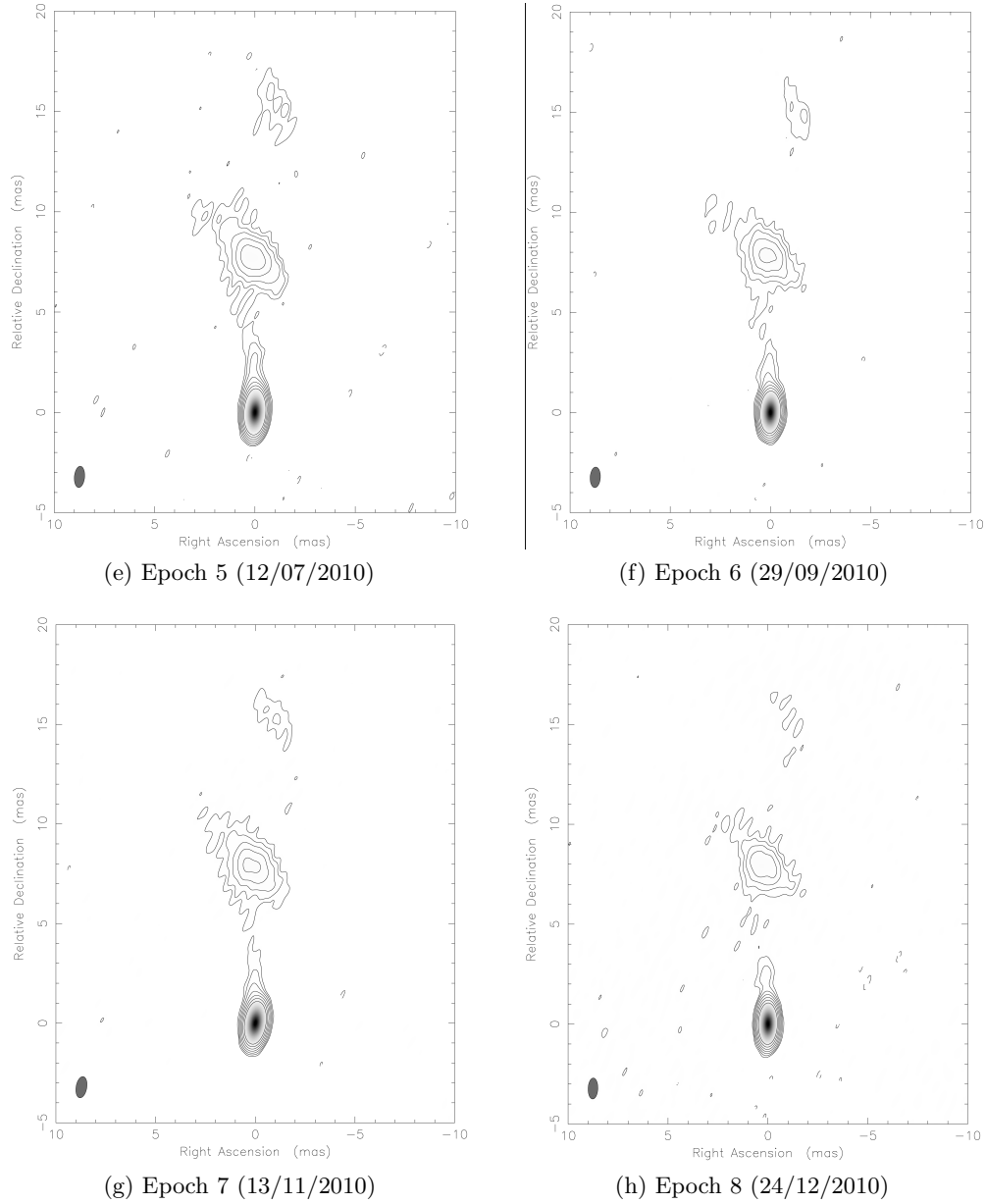


Figure 4.1: The brightness distribution maps for 4C+21.35 over the 8 studied epochs. See Table 4.1 for information about flux, beam size and contour levels.

Epoch	Beam FWHM (mas)	Peak intensity [Jy/beam]	Contour levels [Jy/beam]
1	1.06×0.491	0.793	$0.0015 \times (-0.8 \dots 51.2)$
2	1×0.567	0.784	$0.001 \times (-0.8 \dots 51.2)$
3	1.02×0.572	0.886	$0.001 \times (-0.8 \dots 51.2)$
4	0.933×0.537	1.04	$0.001 \times (-0.8 \dots 51.2)$
5	1.07×0.511	1.62	$0.0015 \times (-0.8 \dots 51.2)$
6	1.02×0.511	1.65	$0.002 \times (-0.8 \dots 51.2)$
7	1.08×0.54	1.44	$0.002 \times (-0.8 \dots 51.2)$
8	1.05×0.487	1.69	$0.0025 \times (-0.8 \dots 51.2)$

Table 4.1: Parameters for the maps shown in Figure 4.2. Beam size refers to the size of the ideal beam convolved with the clean components to obtain the clean map; Peak intensity is the flux density at the brightest point on the map; Contour levels refer to the values of the contour levels on the map, these increase by powers of 2 and are multiplied by an initial minimum value chosen (visually) for the most detailed image without picking up too much noise.

amplitude data is well calibrated.

4.2 Model components

The MODELFITTING of gaussian components to the distinguishable features of 4C+21.35 was carried out as described in section 3.2. Initially, a large number of components were added to the model (around 15 for each epoch) but it was found that deleting certain spurious components did not affect the fit in any considerable way - there were indeed too many components. After a series of trial-and-error approaches, eight components seemed to provide an accurate model for the brightness distribution of Epoch 1. These initial eight components were then used as the starting model for the subsequent epoch, and so forth for further maps.

It was necessary to add a component to the model from Epoch 3 onwards due to the apparition of an additional bright feature during the MODELFIT. This also improved the χ^2 from 1.11 to 0.89, therefore the 9-component model was kept as the starting model for Epoch 4. The components were labelled in ascending order, with the core component as component 1, the next two components 2a and 2b (to distinguish the component appearing in Epoch 3) and then adding one all the way to ten. This is illustrated in Table 4.2, where a sample of the component data from one Epoch is shown.

The model parameters are: position (given by polar coordinates), flux density, component diameter, angle of the primary axis and frequency. The only parameters of interest to this study were the position and flux density, however, with the component size playing a role in the uncertainty estimate.

The raw component data, outputted in the form of a text file, was piped into excel using a perl script I wrote, and the positions of the components were then plotted. Crucially,

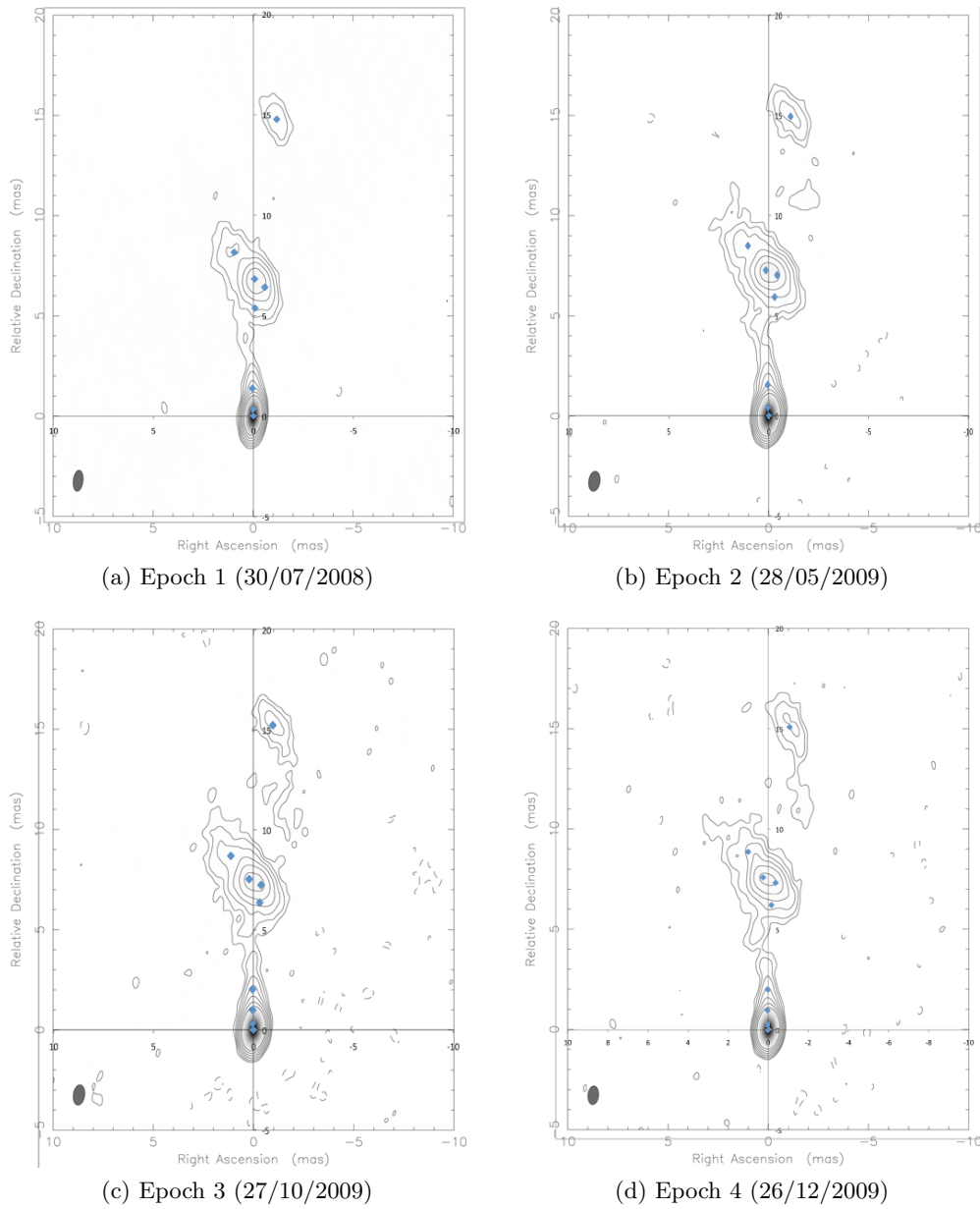


Figure 4.2: Brightness maps with positions of gaussian MODELFITTED components plotted in blue. The apparition of an extra component near the core is clearly visible in Epoch 3. Note that the positions plotted here are simply the centers of the components, and that the components have a finite size determined by the modelled feature. Component size is also taken into account when estimating the error in position. For all component parameters see appendix A

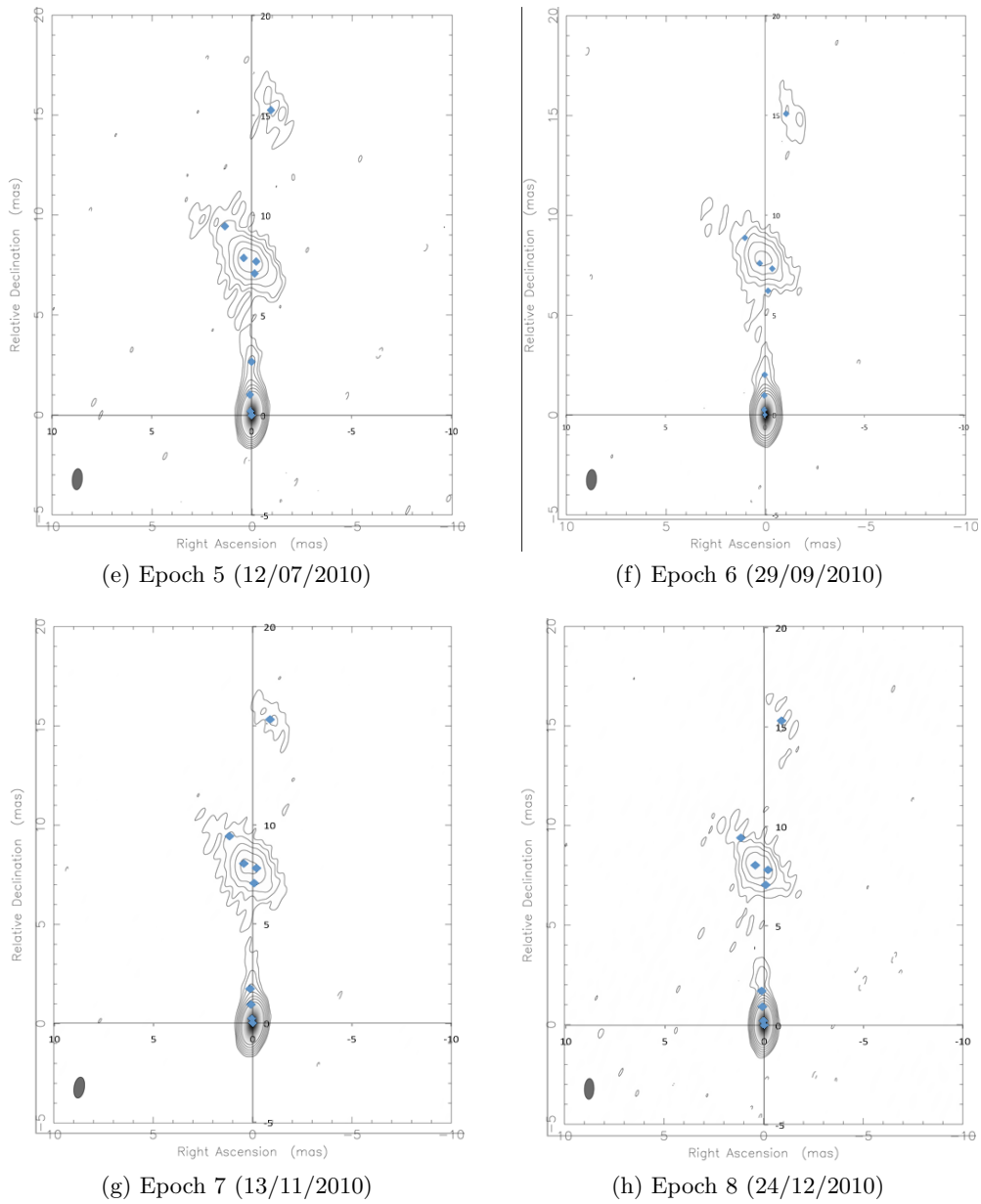


Figure 4.2: Brightness maps with positions of gaussian MODELFITTED components plotted in blue. The apparition of an extra component near the core is clearly visible in Epoch 3. Note that the positions plotted here are simply the centers of the components, and that the components have a finite size determined by the modelled feature. Component size is also taken into account when estimating the error in position. For all component parameters, see appendix A.

Component	Flux density [Jy/beam]	x [mas]	y [mas]	r [mas]
1	1.47603	0	0	0
2a	0.254602	0.04079481	0.230395721	0.233979496
2b	0.00764151	0.09264392	0.936742365	0.941312464
3	0.0102678	0.129904853	1.729378455	1.734250591
4	0.0411841	-0.073204073	7.05713266	7.057512325
5	0.0206318	-0.19042531	7.815140763	7.81746039
6	0.0571212	0.450483888	8.047820007	8.060418265
7	0.0211476	1.172357174	9.425789255	9.498416943
8	0.0130557	-0.871956113	15.31481531	15.33961784

Table 4.2: Component parameters for Epoch 8. There are 9 components labeled in ascending order of r , which is given by $r = \sqrt{x^2 + y^2}$, and it can be noted that the core component is a lot brighter than all the others; this makes for easy use as a coordinate origin across all epochs, as the core of the jet is assumed not to move in time (rather, the brightest component is in the vicinity of the accretion disk and is continually giving off the same amount of radiation).

the position of the core component (the brightest one) was always set to be the origin, which then enabled to have a consistent reference frame across the epochs.

An illustration of the positions of the components, overlaid onto the brightness maps, is shown in Figure 4.2. Visually, the location of the components corresponds very well to brighter features of the map, and there are no obvious discrepancies that would suggest the maps or the models are fundamentally flawed. This can be taken as a further validation of both the imaging process and the MODELFITTING process. Details of all 70 components can be found in Appendix A, and a sample of the component data is shown in Table 4.2.

Error estimation

The estimation of uncertainties involved in the results from this study arises essentially from uncertainties in the MODELFITTING process. Unfortunately, these depend nonlinearly on a large number of parameters including interferometer coverage, thermal noise and the presence of other components; therefore determining the error in the component positions and fluxes given by DIFMAP is an complex process involving detailed statistical analysis that is beyond the scope of this report.

A number of methods have been developed to deal with this issue: Piner et al. (2007) study the component scatter for two pairs of adjoining epochs containing seven sources each, where any difference in the component positions would be due to statistical errors rather than motion due to the closeness of the epochs (separated by 10 and 2 days). They find the scatter to be proportional to the beam size and the flux of the component, with brighter components being determined with greater accuracy.

Homan et al. (2002) study the component flux variability for 12 blazars over 6 epochs, and find that small fluctuations from epoch to epoch, outside a 5 pc radius from the core, rarely exceed 10% of the component flux; the brighter components closer to the core can exhibit up to a 30% variation. They also empirically determine uncertainties in the fluxes of VLBI model components at 15 GHz (using a Monte Carlo simulation and generation of 50,000 artificial data sets), and find an uncertainty of less than 5% of the component flux in a single epoch.

Finally, Lister et al. (2009) study the scatter of 1058 component positions around a best-fit model (given by fitted vector motion, which constructs a vector for the motion across multiple epochs). They find an upper bound on the uncertainty of 0.29 mas (more than 95% of the components have ≤ 0.29 mas uncertainty) and a most probable uncertainty in the range 0.04-0.06 mas. As with Piner et al., the errors are found to be smaller for brighter components. Given that Lister et al. used the same source for their data as this study, the uncertainties adopted will reflect their findings, with ± 0.1 mas used for components not part of the core “grouping” (components 5, 6, 7, 8) and ± 0.05 mas used for the more accurately determined components closer to the core (1, 2a, 2b, 3 and 4).

4.3 Kinematic analysis

Once the components were fitted and their positions determined with respect to a consistent coordinate, they were visually identified across the epochs. This was possible due to the relatively short times between observations, and the absence of large position shifts for any of the components. It was then possible to plot their position against time and thus determine the apparent velocity of each component. The position coordinate used was r , rather than x and/or y , as it is a direct measure of the angular separation from the core. These plots were assembled onto the same graph and can be seen in Figure 4.6.

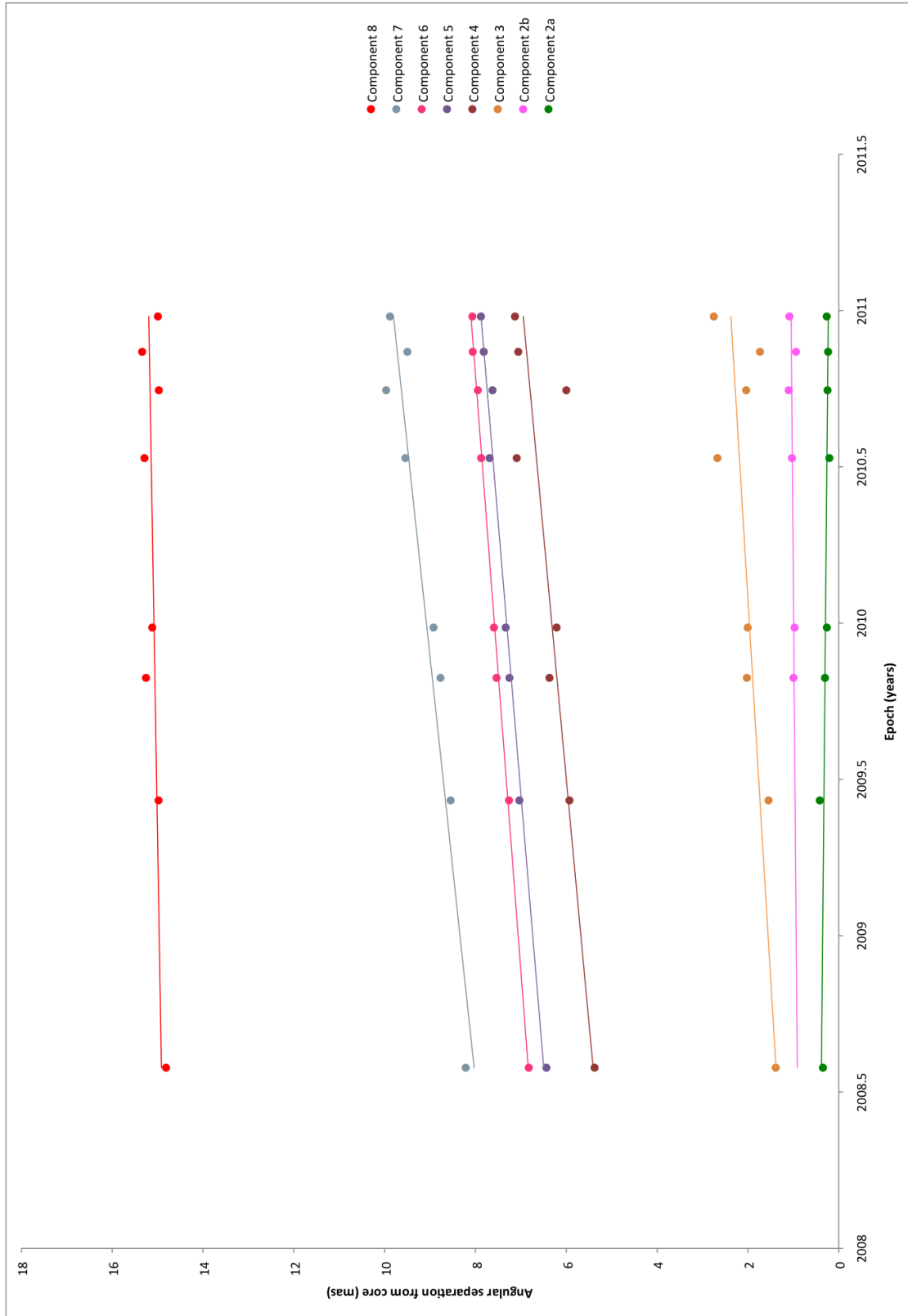


Figure 4.3:

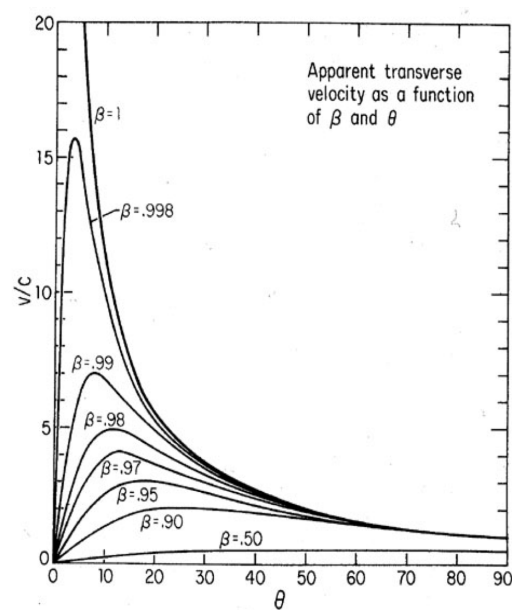


Figure 4.4: An illustrative plot of the observed velocity β_{obs} against the viewing angle θ , plotted for different source velocities β . β_{obs} increases for smaller θ and β approaching 1.

Linear regression was then applied to the position curves, and the coefficients were taken to be the component angular velocities, μ . These are listed in Table 4.3. The uncertainties are derived from the linear regression fit found in Gnuplot. This simple method for deriving the velocities can be considered valid if the motion is assumed to be non-accelerating. From μ , equation 2.14 can be used to find the apparent transverse velocity of the component, using the blazar redshift $z = 0.432$ and angular-size distance $D_a = 5.60$ pc/mas (as cited in section 2.3). These values are also presented in 4.3.

With a maximum component velocity of $\sim 20 c$, the source clearly exhibits superluminal motion. This means that it is possible to use equation 2.9 to find the viewing angle θ and the true component velocity (from β).

Looking at expression 2.9 it can be seen graphically that β_{obs} will reach a maximum for a small θ , and then decrease after that maximum for increasing θ , as can be seen in Figure 4.4. Making the assumption that the maximum observed velocity of the jet is situated at the optimum angle θ_{max} , it is possible to derive a value for θ_{max} . This can be taken as a lower limit on the viewing angle, as smaller angles would mean even larger velocities than the current maximum observed value. The other velocities can then either be due to intrinsic, component specific reasons or simply a larger viewing angle for that particular part of the jet.

Taking the derivative of equation 2.9 with β constant gives:

$$\frac{\beta \cos \theta}{1 - \beta \cos \theta_{\text{max}}} - \frac{(\beta \sin \theta_{\text{max}})^2}{(1 - \beta \cos \theta_{\text{max}})^2} = 0. \quad (4.1)$$

Rearranging and solving for $\cos \theta_{max}$,

$$\cos \theta_{max} = \beta \Rightarrow \sin \theta_{max} = \sqrt{1 - \cos^2 \theta_{max}} = \frac{1}{\gamma}, \quad (4.2)$$

hence

$$\beta_{obs,max} = \beta\gamma = \frac{\beta}{\sqrt{1 - \beta^2}}. \quad (4.3)$$

Finding β is then simply a case of solving the quadratic equation 4.3. For $\beta_{obs,max} = 19.36c$, the equation

$$(-19.36 - 1)\beta^2 + (19.36)^2 = 0 \quad (4.4)$$

has a double root, $\approx \pm 0.998669$.

θ is then given by

$$\theta = \cos^{-1} \beta = 2.956^\circ. \quad (4.5)$$

This very small viewing angle confirms the fact that 4C+21.35 is considered a blazar, what is being observed is a very relativistic, very bright jet moving towards the observer almost head-on.

In turn, the Lorentz factor γ can be determined, where

$$\gamma = \frac{1}{\sqrt{1 - \beta^2}}. \quad (4.6)$$

This evaluates as $\gamma = 19.4$, which will give rise to strong relativistic beaming as given by equation 2.4 (all the more so combined with the small viewing angle). If a further flux or spectral analysis of the source were to be performed (as opposed to the overview of the flux evolution presented below) care must be taken to fully account for the effects of the strong beaming.

For a more thorough measurement of μ , which can take into account any possible acceleration, it would have been necessary to perform velocity vector fits to every component for every epoch, and then use these to determine an average μ for each component. Unfortunately time and resource constraints meant that the less accurate method of the linear gradient was used.

The vector-fit method was used by Lister et al. (2009) while determining the component velocities and accelerations for 127 different jets, including 4C+21.35. This was undertaken for 16 epochs from 1996 to 2007 (the last epoch is the observation immediately preceding epoch 1 in this report), and as such it is interesting to compare the component evolution over both sets of data, and see if they “match up”. The Lister data and the

Component	μ [mas/yr]	v_{obs} [units of c]	R^2 regression fit
8	0.117	3.06	0.272
7	0.74	19.36	0.905
6	0.525	13.74	0.996
5	0.576	15.08	0.983
4	0.641	16.77	0.68
3	0.414	10.83	0.49
2b	0.056	1.46	0.178
2a	-0.062	-1.62	0.574

Table 4.3: The derived velocity parameters for the individual components, found using equation 2.14.

data from this report are plotted in Figure 4.5, where the ‘x’ components and dotted line fits are for the Lister components, and the solid components and lines are for the report components.

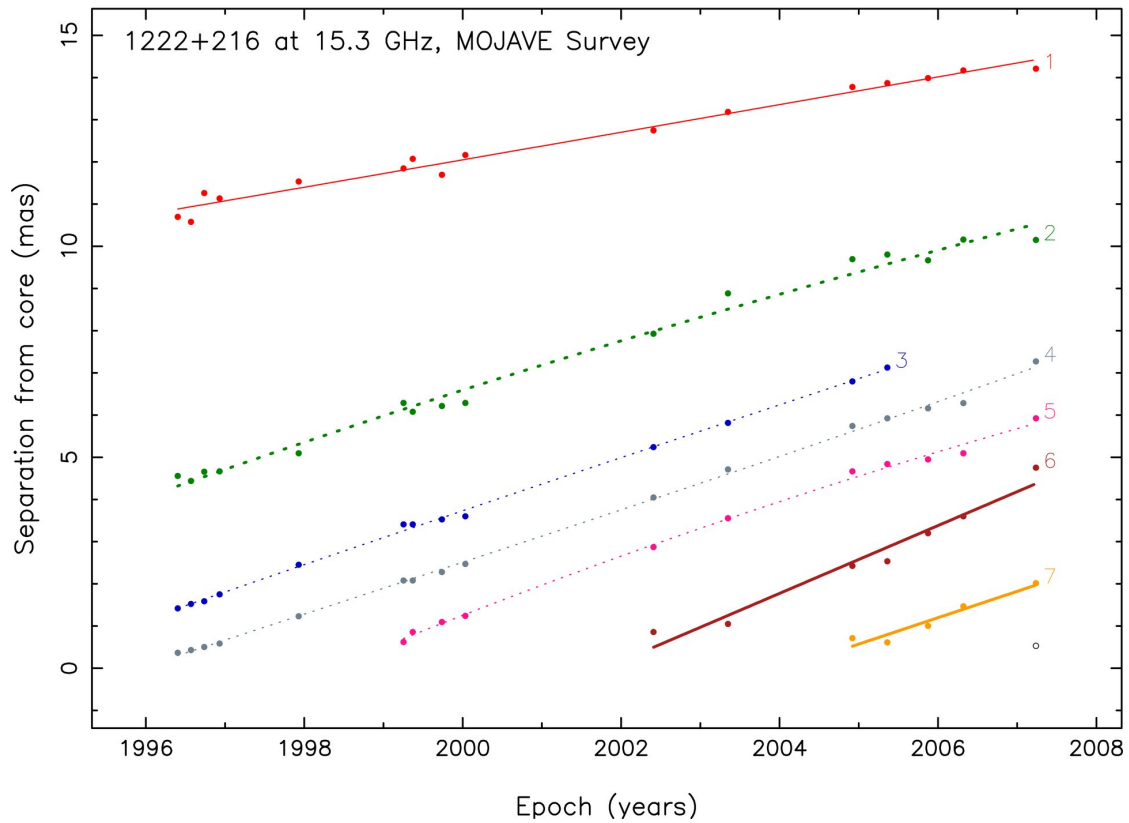


Figure 4.5: Plot of angular distance from core for components of 4C+21.35 (referred to as 1222+216). Dotted line fits represent accelerated motion, whereas solid lines represent a fit to non-accelerated motion. Taken from the MOJAVE kinematic analysis, Lister et al. (2009).

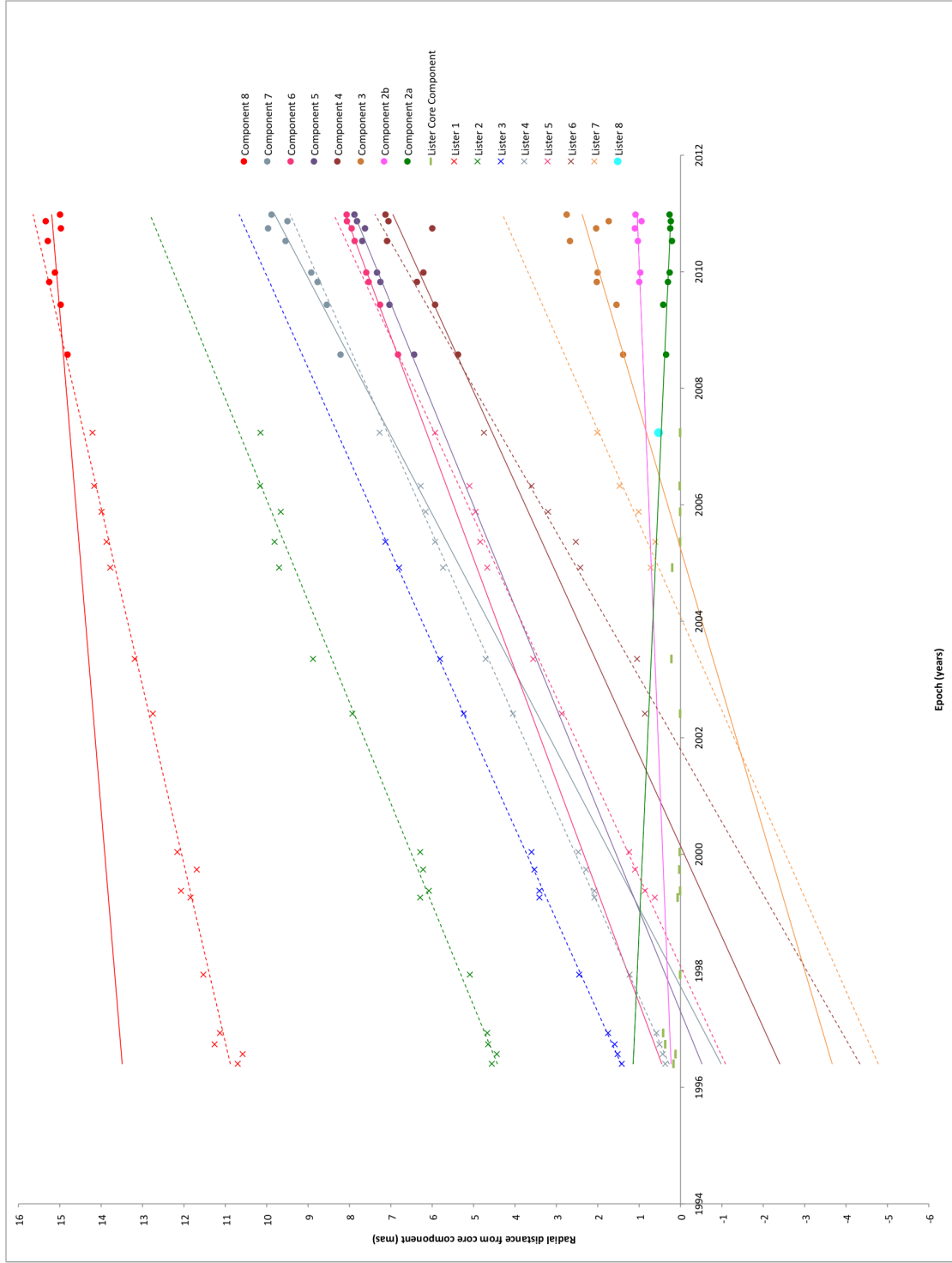


Figure 4.6: A combination of the plots from Figure 4.6 and Figure 4.5, we can now see the evolution of the components over 24 epochs (16 for Lister et al., 8 for this study). Certain components seem to correspond (Components 8,7,6 and 4 all seem to have clear counterparts in the past), one component seems to have been created (component 2b) and two seem to have vanished (Lister components 2 and 3). Furthermore, for some components it is not immediately obvious as to what has happened (component 5, 3 and 2a). These are discussed in the quantitative analysis of the jet.

As Figure 4.6 shows, there is considerable evolution of the components within the jet. Some appear to have longer “lifetimes” than others, some seem to disappear, others are created. It becomes evident that further information is needed, and this was provided by the evolution of the component flux densities with time. These are shown in Figure 4.7 for both Lister’s components and for the later epochs studied here.

The first thing that strikes the eye is the behaviour of the core component: after peaking locally at the early epochs, the flux descends sharply, rises to about a quarter of the amplitude of the first peak, and then rises again sharply after epoch 3, and seems to keep increasing after epoch 8.

The other components, however, all have decreasing flux with time, save component 2a, which starts rising after epoch 3 just like the core.

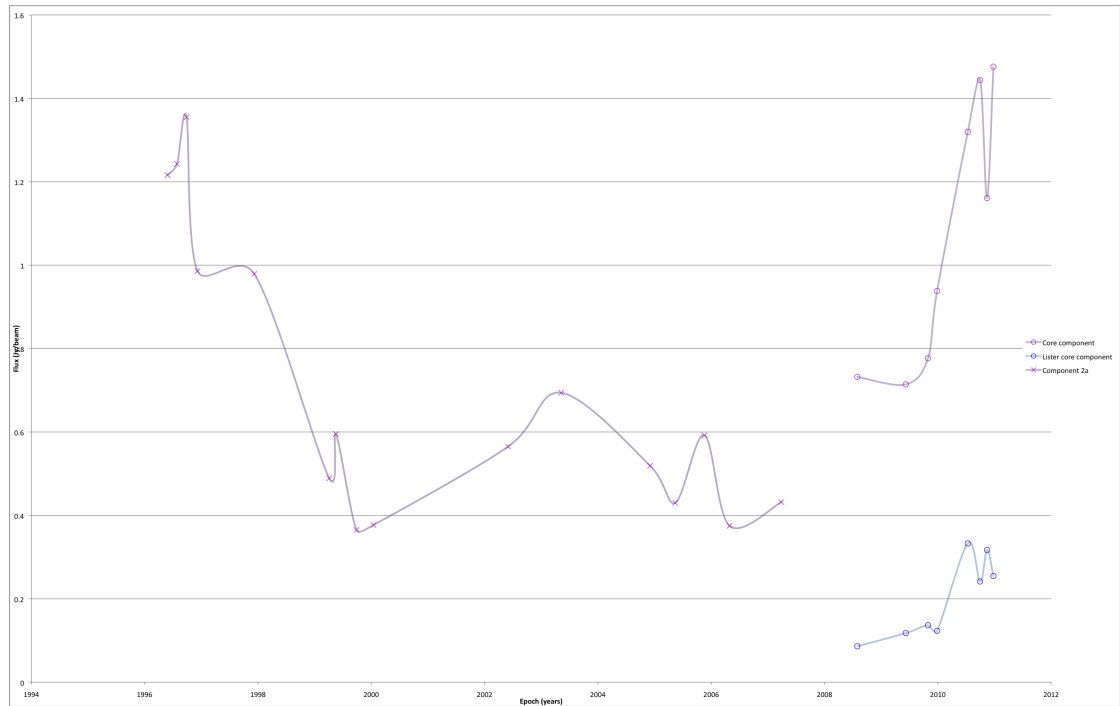
Looking at the overall picture in more detail, and using the flux measurements, we can see that :

- Component 8 and Lister’s component 1 seem to correspond to the same component. The slope of the linear fit on Lister’s epochs is steeper, possibly indicating that the component has begun to slow down from Epoch 4 onwards.
- Lister components 2 and 3 do not have any corresponding components in this study. However, it can be seen that Lister 3 was not present for the last 3 epochs of the data sample, and Lister 2 seemed to stagnate in position during the last two epochs of the sample. These components are in fact seen to have vanishing flux (~ 0.008 Jy/beam for the last epoch of component Lister 2 and 0.016 Jy/beam for the last epoch of Lister 3), and the most probable conclusion to draw would be that they have died out and cannot be distinguished from the background noise any more.
- Component 7 and Lister component 4 also seem to be one and the same. This time Lister’s slope is not as steep as the slope on the more recent components, although this can be explained by the fact that this component had been found to present accelerated motion in the original study (dotted line in Figure4.5).
- Components 5 and 6, and Lister component 5, form an intriguing trio. Indeed, both 5 and 6 could conceivably correspond to Lister 5. Both components also seem extremely bunched together, at times coming between 0.2 mas of each other. After the plots were made and the data was inspected, a new model fit removing one of the two components was tried, but this was to no avail: both components were necessary to produce a satisfying fit. Another possible explanation was then found: components 5 and 6 could be the result of Lister 5 “splitting” into two distinct bright features somehow. A look at the flux data, though, discredits this hypothesis: the flux for Lister 5 at its final epoch is more than twice as large as that of component 5, but smaller than the flux of component 6, at epoch 1.
- Component 4 and Lister component 6 seem to correspond to each other; as with

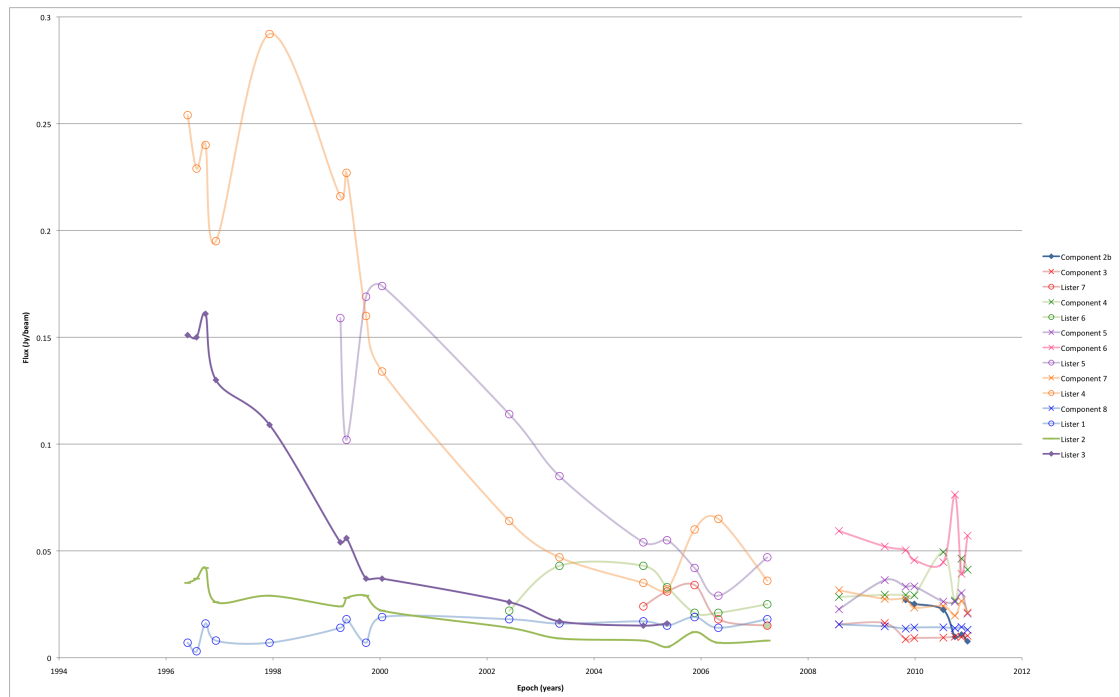
component 8 the slope is steeper for the Lister epochs, indicating a possible slow-down.

- Component 3 and Lister component 7 follow almost parallel slopes while moving away from the core, however they do not seem to be the same component. Looking at the flux shows a comparatively small value of 0.015 for the final epoch of the Lister component, of the same order as Lister 3 before it “disappeared”. It is therefore possible that this also happened for Lister 7. However, Lister 7 could also display complex motion, forming a “standing shock” or stationary knot due to internal shocks (the existence of which has been established by Gomez et al. (1995) and many others), receding, and then moving back outwards. While rare, such complex behaviour has been observed in the case of two components close together by Alberdi et al. (2000) and is a possibility.
- The interpretation of Component 2b is a fairly straightforward one: it appeared between epochs 2 and 3, i.e., between May 2009 and October 2009, close to the core component and component 2a. While the mechanism behind new components appearing is currently very unclear, the timing of the appearance seems to coincide with the beginning of the blazar flaring across the radio and γ -ray spectra (as mentioned in section 2.3). This is in accordance with previous findings by Chatterjee et al. (2009) and Marscher et al. (2002), where the ejection of a bright, superluminal knot from the core is strongly correlated with a preceding X-ray dip and a subsequent radio flare.
- Component 2a bucks the trend and displays apparent inward motion. However, in the MOJAVE study already extensively referenced (Lister et al., 2009), the authors present possible explanations for this phenomenon. This particular component is extremely close to the core and appears to oscillate around a 0.25 mas angular separation from the core. This is at the limit of the VLBA resolution, however, and the component is likely a stationary feature at the edge of the core.

The relativistic jet of 4C+21.35 behaves like a typical gamma-loud blazar jet, with a high Lorentz factor, high radio intensity due to Doppler boosting of the synchrotron emission and a very small angle of sight; these are all factors which agree with the unified AGN model presented in section 2.2. Furthermore, the ejection of a new core component is seen to coincide with the early stages of γ - and radio flaring of the blazar as reported by the Fermi-LAT telescope in April 2009, December 2009 and April 2010.



(a) Flux of core component from Lister and this report, as well as of component 2a.



(b) Fluxes of all other core components. The two “extinguished” components from Lister, as well as the new component, are plotted with stronger lines.

Figure 4.7: Flux evolution of all components over time. There is a gap in the lines delimiting the Lister epochs and the ones covered in this report. For greater clarity, the large fluxes were plotted separately (the cores and one other component) - note the scale change. The data agrees with the radio flares reported by UMRAO (Figure 2.11).

Chapter 5

Summary and Conclusions

The purpose of this study was to investigate the relativistic jet in the blazar 4C+21.35. Blazars are a class of Active Galactic Nuclei (AGN), a broad category of very bright extragalactic objects. These can take a wide range of appearances, from the very bright, and compact, blazars like the source in this report, to the extended lobes of a radio galaxy. However, there is an underlying model unifying these various forms; they are theoretically structurally identical, but their aspect depends on the angle they are viewed from. The key (and most visible) feature of such AGNs are the jets of plasma emitted at relativistic speeds from the hypothesized supermassive black hole and accompanying accretion disk at the center of every AGN. The strong brightness of the AGN sources is attributed to the non-thermal emission of synchrotron radiation from the jet as it is accelerated by a magnetic field thought to be generated by the accretion disk.

The AGN subclass of blazars is characterised by a relatively flat spectrum encompassing all wavebands from radio to γ -ray, as well as the compactness and brightness already mentioned. A positive correlation between γ -ray activity and blazar jet speed has been established (Lister et al., 2009), where the relativistic speeds involved imply apparent superluminal motion from the jet (due to the specific geometry of the observations, the source seems to be moving at faster-than-light speeds. Furthermore, increase of radio and γ -ray flux can both be linked to the ejection of a new bright component from the core into the jet (Chatterjee et al. 2009, for example) indicating a changing morphology worth investigating. With this in mind, the source was chosen on the basis of recent flaring activity in the radio and γ -ray wavebands, and because it was one of the AGNs currently monitored by the VLBA through the MOJAVE project: there was regular, well calibrated data available for 8 epochs from 2008 to 2010.

The data was obtained using the Very Long Baseline Interferometry technique, which involves combining the data of an array of radio telescopes to obtain a very high resolution image of the observed source. VLBI works by sampling the complex visibility (Fourier transform of the brightness distribution) of the source one time for every pair of interferometers, or every “baseline” (Burke and Graham-Smith, 2002). The judicious

combining of baselines to sample the visibility as completely as possible and obtain a faithful image is known as aperture synthesis. Using very large baselines, such as is the case for the VLBA, the effective aperture of the interferometer array can reach thousands of kilometers. This enables a very high resolution image to be formed. 4C+21.35 was observed at 2 cm wavelength (15.3 GHz) for all 8 epochs, which corresponded to resolution of 0.5 parsecs. Knowing that the angular-size distance of the source is 5.60 pc/mas, this permitted imaging of the blazar at parsec length scales. At this scale, the relativistic jet (there is only one visible, as it is viewed head-on) is very collimated and bright, and moves at extremely fast speeds.

The visibility data provided by the MOJAVE project was treated so as to extract the source brightness and make maps of the brightness distribution. On a decaparsec scale, 4C+21.35 was found to present as a single bright jet extending northwards for about 15 mas from a very bright core. Furthermore, the jet seems to be increasing in size as various features move away from the core. For a more quantitative analysis, it was necessary to fit a model to the source data. Gaussian components, characterised by position, size and flux parameters, were fitted to bright spots in the visibility data. Individual components were then identified over the various epochs, using the brightest component or “core” component as a reference point. 8 , then 9 components were fitted for each epoch, there having been the apparition of a new component between the second and third epoch (Figure 4.2).

Plotting component position versus time, and extracting the slope of a linear fit to the curves, yielded the apparent radial velocity of each component for the studied period (using the assumption that the velocity is constant over time)(Figure 4.6). The maximal velocity found was for the second farthest-component from the core, as $19.36 \pm something$. This was then used to calculate the minimal viewing angle that would yield such a speed, according to the equation describing superluminal motion. This angle was found to be $2.96^\circ \pm something$, and the corresponding Lorentz factor was $19.38 \pm something$. These all indicated a highly beamed, relativistic source, and fit perfectly within the accepted AGN model for such objects.

Further comparative analysis was then performed using the data provided by Lister et al. (2009), who had imaged - and performed a kinematic analysis on - the same source, but for previous epochs dating back to 1996. The data from this report was found to be in agreement with the previous data, with 5 components “matching up”, two components from Lister presumably passing below the detection threshold, thereby “extinguishing”, and a new component appearing in the new data

The component flux over time was also plotted, as an aid to comparing sources from the two studies and to see if the data agreed with existing observations. The flux of the core component was by far the highest, generally an order of magnitude above the other components, and its evolution was consistent with observations made by the Michigan Radio Astronomy Observatory (Figures 4.7,radiolightcurves). A further look at the timescales involved shows that the radio flux starts to increase rapidly between epochs

2 and 3, precisely at the time of apparition of the new component. This by itself agrees with the correlation previously found by others (as cited above) between component apparition and flux increase. Further relating the radio increase with the γ -ray increase, it is noteworthy that the first flare occurred in April 2009, or about a month before epoch 2. The second flare occurs in December 2009, by which time the component has been ejected. The occurrence of the γ flaring, preceding the increase in radio intensity, appears to fit the results of Pushkarev et al. (2010), where a delay between γ - and radio emission is found in a sample of 183 radio and γ -bright blazars (of which this source was an element). The relationship between γ and radio also agrees with the results of Kovalev et al. (2009), who find that AGN jets tend to be found in a more active state a few months after Fermi-LAT detection of a strong γ -ray emission.

The main qualitative result of the new core component corresponding to flux increase could have a very interesting implication with respect to the morphology of the jet. Looking again at the brightness maps (Figure 4.2, there are three main “groupings” of flux: the one around the core, the one centered about 8 mas from the core, and the one at ~ 15 mas from the core. The further away from the core, the less bright they get, as is easily visible from the contour map. Considering now Figures 4.7 and ??, it can be seen that there was a previous peak of flux in 1996 - which could correspond to the emission of Lister component 4, identified as component 7, the current fastest component, in the studied images. Component 7 is the furthest away (and presumably the first created) of the components in the second “flux grouping” as described above. It is imaginable that Lister component 1, our component 8, is the last trace of a component ejection and flare that occurred during the 1980s (by simple linear extrapolation).

Unfortunately, no γ -ray data exists for the 1996 flare, and it is impossible to see if there was an accompanying flare. It would, however, be of great interest to continue monitoring the source at the 2 cm and γ wavelengths and see how the current “core grouping” evolves, as well as searching for further flaring and component ejection in the future. Additionally, as VLBI resolution continues to grow and the arrays get more sensitive (notably with the Square Kilometer Array currently in planning), more light will be shed on the formation processes of new components in relativistic blazar jets.

Bibliography

- A. Alberdi, J. L. Gómez, J. M. Marcaide, A. P. Marscher, and M. A. Pérez-Torres. 4C 39.25: Witnessing the interaction between a moving and a stationary component. *A&A*, 361:529–534, Sept. 2000.
- R. Antonucci. Unified models for active galactic nuclei and quasars. *ARA&A*, 31:473–521, 1993. doi: 10.1146/annurev.aa.31.090193.002353.
- W. B. Atwood, A. A. Abdo, M. Ackermann, W. Althouse, B. Anderson, M. Axelsson, L. Baldini, J. Ballet, D. L. Band, G. Barbiellini, and et al. The Large Area Telescope on the Fermi Gamma-Ray Space Telescope Mission. *ApJ*, 697:1071–1102, June 2009. doi: 10.1088/0004-637X/697/2/1071.
- W. Baade and R. Minkowski. Identification of the Radio Sources in Cassiopeia, Cygnus a, and Puppis a. *ApJ*, 119:206–+, Jan. 1954. doi: 10.1086/145812.
- S. Bhatnagar. *Radio Study of Galactic Supernova Remnants and the Interstellar Medium*. PhD thesis, University of Pune, 2001.
- R. D. Blandford and D. G. Payne. Hydromagnetic flows from accretion discs and the production of radio jets. *MNRAS*, 199:883–903, June 1982.
- B. F. Burke and F. Graham-Smith. *An Introduction to Radio Astronomy*. Cambridge University Press, second edition, 2002.
- M. Camenzind. Relativistic Outflows from Active Galactic Nuclei. *Mem. Soc. Astron. Italiana*, 76:98–+, 2005.
- C. Chang. *Active Galactic Nuclei throughout the Spectrum: M 87, PKS 2052?47, and the MOJAVE sample*. PhD thesis, Max-Planck-Institut für Radioastronomie, 2010.
- R. Chatterjee, A. P. Marscher, S. G. Jorstad, A. R. Olmstead, I. M. McHardy, M. F. Aller, H. D. Aller, A. Lähteenmäki, M. Tornikoski, T. Hovatta, K. Marshall, H. R. Miller, W. T. Ryle, B. Chicka, A. J. Benker, M. C. Bottorff, D. Brokofsky, J. S. Campbell, T. S. Chonis, C. M. Gaskell, E. R. Gaynullina, K. N. Grankin, C. H. Hedrick, M. A. Ibrahimov, E. S. Klimek, A. K. Kruse, S. Masatoshi, T. R. Miller, H.-J. Pan, E. A. Petersen, B. W. Peterson, Z. Shen, D. V. Strel’nikov, J. Tao, A. E.

- Watkins, and K. Wheeler. Disk-Jet Connection in the Radio Galaxy 3C 120. *ApJ*, 704:1689–1703, Oct. 2009. doi: 10.1088/0004-637X/704/2/1689.
- M. H. Cohen, R. P. Linfield, A. T. Moffet, G. A. Seielstad, K. I. Kellermann, D. B. Shaffer, I. I. K. Pauliny-Toth, E. Preuss, A. Witzel, and J. D. Romney. Radio sources with superluminal velocities. *Nature*, 268:405–409, Aug. 1977. doi: 10.1038/268405a0.
- N. J. Cooper, M. L. Lister, and M. D. Kochanzyk. MOJAVE: Monitoring of Jets in Active Galactic Nuclei with VLBA Experiments. III. Deep VLA Images at 1.4 GHz. *ApJS*, 171:376–388, Aug. 2007. doi: 10.1086/518654.
- D. F. Falla and M. J. Floyd. Superluminal motion in astronomy. *European Journal of Physics*, 23(1):69, 2002. URL <http://stacks.iop.org/0143-0807/23/i=1/a=310>.
- B. L. Fanaroff and J. M. Riley. The morphology of extragalactic radio sources of high and low luminosity. *MNRAS*, 167:31P–36P, May 1974.
- G. Fossati, L. Maraschi, A. Celotti, A. Comastri, and G. Ghisellini. A unifying view of the spectral energy distributions of blazars. *MNRAS*, 299:433–448, Sept. 1998. doi: 10.1046/j.1365-8711.1998.01828.x.
- J. Frank, A. King, and D. Raine. *Accretion power in astrophysics*. Cambridge University Press, 2002.
- J. L. Gomez, J. M. A. Marti, A. P. Marscher, J. M. A. Ibanez, and J. M. Marcaide. Parsec-Scale Synchrotron Emission from Hydrodynamic Relativistic Jets in Active Galactic Nuclei. *ApJ*, 449:L19+, Aug. 1995. doi: 10.1086/309623.
- S. E. Healey, R. W. Romani, G. B. Taylor, E. M. Sadler, R. Ricci, T. Murphy, J. S. Ulvestad, and J. N. Winn. CRATES: An All-Sky Survey of Flat-Spectrum Radio Sources. *ApJS*, 171:61–71, July 2007. doi: 10.1086/513742.
- J. A. Högbom. Aperture Synthesis with a Non-Regular Distribution of Interferometer Baselines. *A&AS*, 15:417–+, June 1974.
- D. C. Homan, R. Ojha, J. F. C. Wardle, D. H. Roberts, M. F. Aller, H. D. Aller, and P. A. Hughes. Parsec-Scale Blazar Monitoring: Flux and Polarization Variability. *ApJ*, 568:99–119, Mar. 2002. doi: 10.1086/338701.
- K. G. Jansky. Radio Waves from Outside the Solar System. *Nature*, 132:66–+, July 1933. doi: 10.1038/132066a0.
- W. Junor, J. A. Biretta, and M. Livio. Formation of the radio jet in M87 at 100 Schwarzschild radii from the central black hole. *Nature*, 401:891–892, Oct. 1999. doi: 10.1038/44780.
- K. I. Kellermann, R. Sramek, M. Schmidt, D. B. Shaffer, and R. Green. VLA observations of objects in the Palomar Bright Quasar Survey. *AJ*, 98:1195–1207, Oct. 1989. doi: 10.1086/115207.

- Y. Y. Kovalev, H. D. Aller, M. F. Aller, D. C. Homan, M. Kadler, K. I. Kellermann, Y. A. Kovalev, M. L. Lister, M. J. McCormick, A. B. Pushkarev, E. Ros, and J. A. Zensus. The Relation Between AGN Gamma-Ray Emission and Parsec-Scale Radio Jets. *ApJ*, 696:L17–L21, May 2009. doi: 10.1088/0004-637X/696/1/L17.
- J. M. Krolik. *Active Galactic Nuclei*. Princeton University Press, 1999.
- M. L. Lister, H. D. Aller, M. F. Aller, M. H. Cohen, D. C. Homan, M. Kadler, K. I. Kellermann, Y. Y. Kovalev, E. Ros, T. Savolainen, J. A. Zensus, and R. C. Vermeulen. MOJAVE: Monitoring of Jets in Active Galactic Nuclei with VLBA Experiments. V. Multi-Epoch VLBA Images. *AJ*, 137:3718–3729, Mar. 2009. doi: 10.1088/0004-6256/137/3/3718.
- M. L. Lister, M. H. Cohen, D. C. Homan, M. Kadler, K. I. Kellermann, Y. Y. Kovalev, E. Ros, T. Savolainen, and J. A. Zensus. Mojave: Monitoring of jets in active galactic nuclei with vlba experiments. vi. kinematics analysis of a complete sample of blazar jets. *The Astronomical Journal*, 138(6):1874, 2009. URL <http://stacks.iop.org/1538-3881/138/i=6/a=1874>.
- M. L. Lister, D. C. Homan, M. Kadler, K. I. Kellermann, Y. Y. Kovalev, E. Ros, T. Savolainen, and J. A. Zensus. A Connection Between Apparent VLBA Jet Speeds and Initial Active Galactic Nucleus Detections Made by the Fermi Gamma-Ray Observatory. *ApJ*, 696:L22–L26, May 2009. doi: 10.1088/0004-637X/696/1/L22.
- A. Lobanov. Physical properties of blazar jets from VLBI observations. *ArXiv e-prints*, Oct. 2010.
- A. P. Marscher, S. G. Jorstad, J.-L. Gómez, M. F. Aller, H. Teräsranta, M. L. Lister, and A. M. Stirling. Observational evidence for the accretion-disk origin for a radio jet in an active galaxy. *Nature*, 417:625–627, June 2002.
- I. F. Mirabel and L. F. Rodríguez. A superluminal source in the Galaxy. *Nature*, 371:46–48, Sept. 1994. doi: 10.1038/371046a0.
- M. Miyoshi, J. Moran, J. Herrnstein, L. Greenhill, N. Nakai, P. Diamond, and M. Inoue. Evidence for a black hole from high rotation velocities in a sub-parsec region of NGC4258. *Nature*, 373:127–129, Jan. 1995. doi: 10.1038/373127a0.
- M. Nakamura and D. L. Meier. Unsolved Problems of AGN Jets in Sub Parsec Scale: Acceleration, Collimation, and Stability Properties. In Y. Hagiwara, E. Fomalont, M. Tsuboi, & M. Yasuhiro, editor, *Approaching Micro-Arcsecond Resolution with VSOP-2: Astrophysics and Technologies*, volume 402 of *Astronomical Society of the Pacific Conference Series*, pages 357–+, Aug. 2009.
- T. J. Pearson. Non-Imaging Data Analysis. In J. A. Zensus, P. J. Diamond, & P. J. Napier, editor, *Very Long Baseline Interferometry and the VLBA*, volume 82 of *Astronomical Society of the Pacific Conference Series*, pages 268–+, 1995.

- T. J. Pearson, M. C. Shepherd, G. B. Taylor, and S. T. Myers. Automatic Synthesis Imaging with Difmap. In *American Astronomical Society Meeting Abstracts*, volume 26 of *Bulletin of the American Astronomical Society*, pages 1318–+, Dec. 1994.
- A. A. Penzias and R. W. Wilson. A Measurement of Excess Antenna Temperature at 4080 Mc/s. *ApJ*, 142:419–421, July 1965. doi: 10.1086/148307.
- B. G. Piner, M. Mahmud, A. L. Fey, and K. Gospodinova. Relativistic Jets in the Radio Reference Frame Image Database. I. Apparent Speeds from the First 5 Years of Data. *AJ*, 133:2357–2388, May 2007. doi: 10.1086/514812.
- A. B. Pushkarev, Y. Y. Kovalev, M. L. Lister, and T. Savolainen. Jet opening angles and gamma-ray brightness of AGN. *A&A*, 507:L33–L36, Nov. 2009. doi: 10.1051/0004-6361/200913422.
- A. B. Pushkarev, Y. Y. Kovalev, and M. L. Lister. Radio/Gamma-ray Time Delay in the Parsec-scale Cores of Active Galactic Nuclei. *ApJ*, 722:L7–L11, Oct. 2010. doi: 10.1088/2041-8205/722/1/L7.
- M. J. Rees. Appearance of Relativistically Expanding Radio Sources. *Nature*, 211: 468–470, July 1966. doi: 10.1038/211468a0.
- M. Rowan-Robinson. On the unity of activity in galaxies. *ApJ*, 213:635–647, May 1977. doi: 10.1086/155195.
- G. B. Rybicki and A. P. Lightman. *Radiative processes in astrophysics*. Wiley, New York, 1979.
- M. C. Shepherd. Difmap: an Interactive Program for Synthesis Imaging. In G. Hunt & H. Payne, editor, *Astronomical Data Analysis Software and Systems VI*, volume 125 of *Astronomical Society of the Pacific Conference Series*, pages 77–+, 1997.
- G. Taylor. *The DIFMAP Cookbook*, 1997.
- A. Thompson, J. Moran, and G. Swenson. *Interferometry and synthesis in radio astronomy*. Wiley, 2001.
- C. M. Urry and P. Padovani. Unified Schemes for Radio-Loud Active Galactic Nuclei. *PASP*, 107:803–+, Sept. 1995. doi: 10.1086/133630.
- N. Vlahakis and A. Königl. Magnetic Driving of Relativistic Outflows in Active Galactic Nuclei. I. Interpretation of Parsec-Scale Accelerations. *ApJ*, 605:656–661, Apr. 2004. doi: 10.1086/382670.
- W. Xu, A. C. S. Readhead, T. J. Pearson, A. G. Polatidis, and P. N. Wilkinson. The First Caltech–Jodrell Bank VLBI Survey. III. VLBI and MERLIN Observations at 5 GHz and VLA Observations at 1.4 GHz. *ApJS*, 99:297–+, Aug. 1995. doi: 10.1086/192189.